ATLAS NOTE

ATLAS-CONF-2013-089

August 24, 2013
Revision: September 30, 2013

Search for strongly produced supersymmetric particles in decays with two leptons at $\sqrt{s} = 8$ TeV

The ATLAS Collaboration

Abstract

This note presents a search for squarks and gluinos in final states containing two isolated electrons or muons using the ATLAS Detector at the LHC in 20.3 fb^{-1} of $\sqrt{s} = 8$ TeV proton-proton collisions. The search uses a set of variables carrying information on the event kinematics both transverse and parallel to the beam line that are sensitive to several topologies expected in Supersymmetry. No excess above the Standard Model expectation is observed, and exclusion limits at 95 % confidence level are set on the visible cross section for the production of new physics within the kinematic requirements of the search. The results are additionally interpreted as lower limits on sparticle masses for various simplified model scenarios concerning the pair-production of gluinos and first and second-generation squarks and a minimal universal extra dimensions model.

A typo was found in the caption and text overlaid on Figures 21-24. The text has been corrected to clarify that the limit is on the production cross section and not the visible cross section.

1 Introduction

Physics processes beyond the Standard Model (BSM) are the target of a range of searches at the Large Hadron Collider (LHC). One of the most popular candidate theories for BSM physics is Supersymmetry (SUSY) [1–9], and SUSY searches comprise a large number of analyses covering a broad variety of final states. The relatively large production cross section of squarks and gluinos at the LHC has motivated dedicated searches for inclusive strong production of SUSY particles (sparticles). In *R*-parity conserving (RPC) models [10–14], gluinos and squarks decay directly, or through cascades, into jets, possibly leptons, and the lightest supersymmetric particle (LSP), which escapes detection and leads to missing transverse momentum ($\vec{E}_{\mathrm{T}}^{\mathrm{miss}}$, and its magnitude $E_{\mathrm{T}}^{\mathrm{miss}}$).

This note presents a search for gluinos and first- and second-generation squarks in events with two isolated leptons, in 20.3 fb^{-1} of $\sqrt{s}$ = 8 TeV data collected in 2012 by the ATLAS detector [15] at the Large Hadron Collider (LHC) [16]. ATLAS has published an extensive range of RPC SUSY searches for strong inclusive sparticle production at the LHC, targeting leptonic [17–19] and fully hadronic [20, 21] final states. The techniques employed by individual analyses vary, resulting in a complementary set of BSM searches. This analysis makes use of a set of kinematic variables that exploits both transverse and longitudinal event information, referred to as the Razor variables [22], in order to select signal-like topologies. This set of kinematic variables, which incorporate longitudinal event information along with traditional event-by-event variables defined in the transverse plane, has been used in previous analyses at ATLAS [23] and CMS [24]. Relative to the previous ATLAS result [23], this analysis has been fully re-optimised to focus on specific signal models described in Section 2.1 and make use of the larger 2012 dataset.

This note is organised as follows. The SUSY models considered and the SM background Monte Carlo (MC) samples employed in the search are described in Section 2. The object reconstruction and event selection are explained in Section 3. Section 4 describes the background estimation methodology, and the uncertainties on the signal and background are explained in Section 5. The backgrounds and signals enter a simultaneous fit, which is detailed in Section 6. Finally, the results of the search and their interpretation in terms of several SUSY models and a minimal extra dimension model [25] are described in Section 7. Conclusions are given in Section 8.

2 SUSY Signal Modelling and Simulated Event Samples

Samples of simulated events are used to optimise the signal selection, estimate the signal yields and aid in the determination of the SM background contributions.

All generated samples are passed through the ATLAS detector simulation [26], based on Geant4 [27]. Additional minimum-bias pp interactions, generated with Pythia 8.160 [28] using the AM2 tune [29] and the leading-order Parton Density Function (PDF) set `MSTW2008LO` [30], are overlaid on all simulated events to reproduce the effect of additional pp collisions in the same bunch-crossing (pile-up). Corrections are made for small differences between, for example the pile-up, object reconstruction, and object identification efficiencies between data and the simulation during the analysis.

2.1 Signal Event Samples

In this analysis simplified models with SUSY-like topologies are studied. These models contain only a subset of SUSY particles and decay chains possible for a complete SUSY signal model. The simplified models considered in this analysis feature direct pair-production of left-handed first-and second-generation squarks ($\tilde{q}$) and gluinos ($\tilde{g}$). In addition, results are also interpreted in a minimal universal extra dimensions (mUED) model [25].
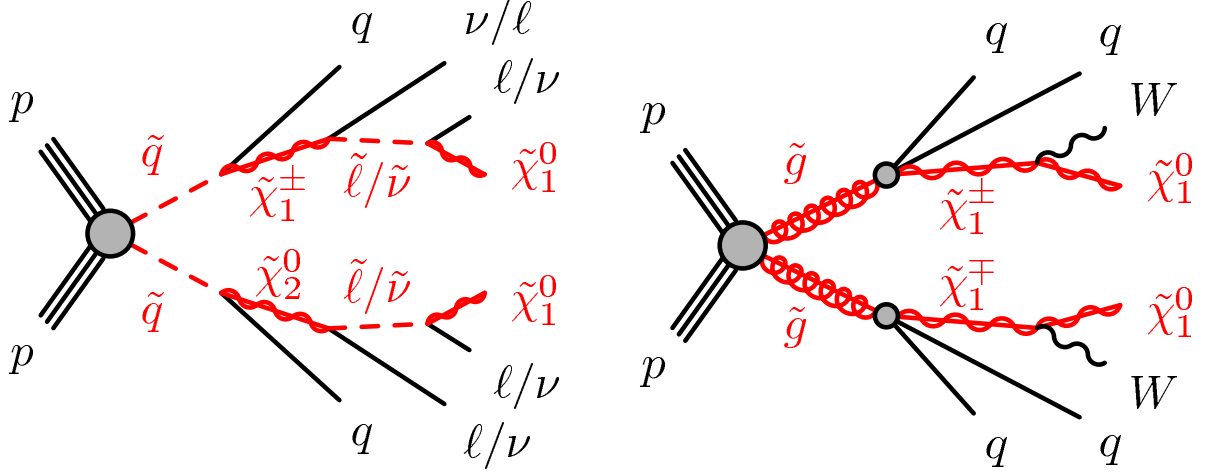
Figure 1: Two example decay diagrams for the simplified models used in this note. On the left, a decay diagram for the simplified model with gluino pair-production and a two-step decay through a chargino and a slepton or sneutrino to the LSP. On the right, a decay diagram for the simplified model with squark pair-production and a one-step decay through a chargino to the LSP.

The simplified models considered are divided into two categories: the "one-step" decay simplified models and the "two-step" models with intermediate sleptons and sneutrinos ($\tilde{\ell}$ and $\tilde{\nu}$). All are models of pair-production of either gluinos or left-squarks, in the latter case with degenerate first and second generation squarks and a decoupled third generation. Since only first and second generation squarks are included, the signal models do not include an appreciable rate of heavy-flavour jets. The heavy SUSY particles decay in a one- or two-step cascade to the LSP, assumed to be the lightest neutralino. Example decay diagrams for the models considered here are shown in Fig. 1.

In the one-step models, gluinos (squarks) are pair-produced, with the gluino (squark) decaying to two (one) quarks and a chargino ($\tilde{\chi}_1^\pm$), assumed to be a pure wino. The chargino subsequently decays to a W-boson and the neutralino LSP ($\tilde{\chi}_1^0$), assumed to be a pure bino. The gluino (squark), chargino, and LSP masses are free parameters in this model, assuming branching ratios of 100 % for each of the steps. Two parameterisations of this model are explored, both making use of the relative chargino-LSP – gluino-LSP (squark-LSP) mass splitting, $x = (m_{\tilde{\chi}_1^\pm} - m_{\tilde{\chi}_1^0})/(m_{\tilde{q}/\tilde{g}} - m_{\tilde{\chi}_1^0})$. The first requires the chargino mass to be exactly halfway between the gluino (squark) and LSP masses. The second fixes the LSP mass at 60 GeV.

In the two-step models, gluinos (squarks) are pair-produced, with the gluino (squark) decaying into two (one) quark(s) and a either a chargino or the next-to-lightest neutralino ($\tilde{\chi}_2^0$), with equal probability for each. The chargino subsequently decays, with equal probability, into either a lepton and a sneutrino or a left-slepton and a neutrino. The neutralino subsequently decays, with equal probability, into either a left-slepton and a lepton or a sneutrino and a neutrino. Finally, the slepton (sneutrino), decays into a lepton (neutrino) and a neutralino LSP. These models are defined such that the masses of the intermediate charginos and neutralinos are equal and are set to be exactly halfway between the gluino (squark) and LSP masses. The slepton and sneutrino masses are then set exactly halfway between the intermediate chargino or neutralino masses and the LSP. All slepton flavours are accounted for in this model and are assumed to be degenerate in mass. The gluino (squark) and LSP masses are free parameters.

All sparticles that do not enter into the decay chains defined in a specific simplified model are assigned a mass of 4.5 TeV, and are effectively decoupled. These models are generated using MADGRAPH5 1.5.4 [31] interfaced with PYTHIA 6.426 [32], using the CTEQ6L1 PDF set [33], as described in Ref. [18].

Signal cross sections are calculated to next-to-leading order in the strong coupling constant, adding the re-summation of soft gluon emission at next-to-leading-logarithmic accuracy (NLO+NLL) [34–38]. The nominal cross section and the uncertainty are taken from an envelope of cross section predictions using different PDF sets and factorisation and re-normalisation scales, as described in Ref. [39]. For the models with squark pair-production, since squark-anti-squark production dominates, only events with opposite-sign leptons enter the signal regions.

This analysis also considers the mUED model, this being the minimal extension to the SM with the addition of one extra spatial dimension. The model is characterised by three parameters: the cut-off scale (Λ), the compactification radius (R_c), and the Higgs boson mass (m_h). The mass spectrum of this model is naturally degenerate. An example decay chain, being that of the Kaluza-Klein (KK) quark to the KK photon (the lightest KK particle), results in a signature similar to that from the SUSY decay chain of the squark to the lightest neutralino discussed earlier. Signal points are generated using Herwig++ 2.5.2 [40] with the CTEQ6L1 PDF set and the CTEQ6L1-UE-EE-3 tune [41]. Events are generated with the Higgs boson mass fixed at 125 GeV.

2.2 Standard Model Event Samples

Physics process	Generator	Cross section (pb)	Cross section calculation order
$t\bar{t}$	Powheg	253	NNLO+NNLL
$Z/\gamma^*(\to \ell\ell)$ + jets ($m_{\ell\ell} > 40$ GeV)	Sherpa	1.2×10^3	NLO
$Z/\gamma^*(\to \ell\ell)$ + jets ($10 < m_{\ell\ell} < 40$ GeV)	Sherpa	371	NLO
Single-top (Wt-chan)	MC@NLO 4.06	22.4	NLO+NLL
WW	Powheg	5.88	NLO
WZ	Powheg	3.68	NLO
ZZ	Powheg	0.987	NLO
$t\bar{t} + W$	MadGraph5	0.232	NLO
$t\bar{t} + Z$	MadGraph5	0.208	NLO
$t\bar{t} + WW$	MadGraph5	0.9×10^{-3}	NLO

Table 1: Simulated background event samples used in this analysis, and the value and order in the strong coupling of the production cross sections. The cross section values shown for Z/γ^* + jets production are listed for a single lepton flavour. The WW cross-section includes leptonic decays of the two W-bosons only, and the cross-section for WZ and ZZ considers only final states with at least two leptons.

The simulated event samples for the SM backgrounds are summarised in Table 1. Herwig 6.520 [42] is used to model the parton shower and fragmentation processes in combination with Jimmy 4.31 [43] for underlying event modelling for the MC@NLO 4.06 [44] samples. Pythia 6 is used for Powheg [45] and AcerMC 3.8 [46], with the latter being used to generate samples used to derive theory uncertainties on the $t\bar{t}$ production background (see Section 5). The CTEQ6L1 PDF sets are used for the AcerMC samples and the CT10 NLO sets [47] are used for the MC@NLO, Sherpa 1.4.1 [48] and Powheg samples. The ATLAS AUET2 underlying event tunes are used [49] for Herwig and Pythia 6. Sherpa uses its own parton shower, fragmentation and underlying event model. The Sherpa Z/γ^* + jets samples are generated with massive b/c-quarks to improve the description of the b-tagging variables. The theoretical cross sections for Z/γ^*+jets are calculated with DYNNLO [50] with the MSTW2008NNLO [51] PDF set. The diboson cross sections are obtained from MCFM [52] using the NLO CT10 PDF set. The $t\bar{t}$ cross section is calculated at NNLO in QCD including next-to-next-to-leading logarithmic (NNLL) soft gluon terms with top++

2.0 [53–58]. The single-top production cross sections are calculated at NLO+NLL accuracy [59–61]. The $t\bar{t} + W/Z$ cross sections are computed at NLO accuracy [62, 63].

3   Object Reconstruction and Event Selection

3.1   Object Reconstruction

Electron candidates are reconstructed from clusters of energy in the calorimeter matched to inner detector tracks. These can be assigned "baseline" or "signal" status. Baseline electrons must satisfy the "medium" selection requirement described in Ref. [64], have transverse energy $E_T > 10$ GeV, reside within pseudo-rapidity $|\eta| < 2.47$ and not be within $1.37 < |\eta| < 1.52$. Signal electrons are further required to be isolated relative to other charged particles, with the quantifier being that the sum of the transverse momenta (p_T) of all charged particle tracks associated with the primary vertex within $\Delta R = \sqrt{\Delta\eta^2 + \Delta\phi^2} < 0.2$ of the electron must be less than 10 % of the electron E_T. The primary vertex is defined as the vertex with the highest $\sum p_T^2$. In addition, signal electrons must satisfy the more stringent track quality, shower shape and matching requirements of "tight" selection criteria [64].

Muon candidates are reconstructed from muon segments matched to inner detector tracks, or otherwise from combined tracks in the inner detector and muon spectrometer [65, 66]. Baseline muons must have $p_T > 10$ GeV and reside within $|\eta| < 2.4$. The isolation requirement imposed on signal muons is that the sum of the p_T of all charged particle tracks associated with the primary vertex within $\Delta R < 0.2$ must be less than 1.8 GeV.

Jets are reconstructed from topological clusters in the calorimeter using the anti-k_t algorithm [67, 68] with a radius parameter of 0.4. They are then calibrated using local cluster weighting (LCW), which accounts for the different calorimeter responses for electrons and hadrons [69]. Jets are pre-selected with $p_T > 20$ GeV, and if these jets do not pass specific jet quality and selection criteria then the event is rejected from selection, so as to remove events from non-collision backgrounds. Signal jets are required to have $p_T > 30$ GeV and reside within $|\eta| < 2.5$. Since the number of jets with $p_T > 30$ GeV is shown to be sensitive to pile-up for this analysis, a cut on the jet vertex fraction (JVF) is placed at $|$JVF$| > 0.25$ for jets with $30 < p_T < 50$ GeV. Here the JVF is the p_T weighted fraction of tracks associated with the jet that are consistent with the primary vertex of the event, and jets with no associated tracks are assigned JVF $= -1$. This cut therefore ensures that the jet originates from the pp collision of interest. Heavy flavour (b-) jets are identified using a multivariate algorithm [70] at a 60 % efficiency working point, for b-jets of $p_T > 25$ GeV.

To avoid the duplication of physics objects in more than one baseline collection an overlap removal procedure is performed. Firstly, if any two baseline electrons lie within a distance of $\Delta R < 0.05$ of one another, the electron with the lowest cluster energy is discarded. Following this, pre-selected jets residing within $\Delta R < 0.2$ of any remaining baseline electron are discarded. Then electrons and muons residing within $\Delta R < 0.4$ of remaining selected jets are discarded. Finally, if any baseline electrons and muons lie within a distance of $\Delta R < 0.01$ of one another, the electron is discarded, and the muon p_T is recalculated to take the electron p_T into account.

Clusters of energy in the calorimeter are calibrated according to the reconstructed object with which they are associated, and they are then used as input into the calculation of missing transverse momentum for each event. This includes all baseline electrons, muons and jets, as well as clusters that are not associated with a reconstructed object.

3.2   Trigger Strategy

Di-lepton triggers are used to select events in data and MC. The offline p_T thresholds for selected leptons are dictated by the specific di-lepton trigger used to select the event in order to ensure that the analysis is

Trigger	Selection	p_T Threshold [GeV]
leading muon	e-μ	14, 18
leading electron	e-μ	14, 8
p_T-asymmetric electron	e-e	25, 8
p_T-symmetric electron	e-e	14, 14
p_T-asymmetric muon	μ-μ	18, 8
p_T-symmetric muon	μ-μ	14, 14

Table 2: Triggers used to select data for this analysis along with their corresponding offline p_T thresholds.

insensitive to the p_T-dependence of the trigger efficiency. A summary of the lepton p_T combinations for different lepton flavour channels is given in Table 2. The two signal leptons in selected di-lepton events are additionally matched to the online trigger objects to within $\Delta R = 0.15$.

3.3   Event Selection

Selected events must have a primary vertex with at least five associated tracks and with a position consistent with the luminous region. In order to remove events due to cosmic rays, events containing a muon in which the transverse and longitudinal impact track parameters are greater than 0.2 mm and 1 mm with respect to the primary vertex, respectively, are vetoed. In addition to this, events containing badly measured, non-isolated muons are also discarded. Finally, events with mis-reconstructed E_T^{miss} as a result of jets pointing towards dead regions of the calorimeter are rejected.

Events selected for this analysis are required to contain exactly two signal leptons, these being two electrons, two muons, or one of each, and no other baseline leptons of $p_T > 10$ GeV within the range $|\eta| < 2.47$. These leptons must pass the trigger requirements described in Section 3.2. Di-leptonic events where the invariant mass of the two leptons is less than 20 GeV are discarded in order to reject low-mass resonances.

3.4   Signal Selection

This analysis makes use of the Razor variables [22] to select signal-like events. These are a set of kinematic variables that exploit the symmetry in the visible portion of sparticle decays when sparticles are produced in pairs. The final state jets and leptons are grouped into two "mega-jets." During this construction all visible objects from one side of the di-sparticle decay are collected together to create a single four-vector, representing the decay products of a single sparticle. The mega-jet construction involves iterating over all possible combinations of the four-vectors of the visible reconstructed objects, with the favoured combination being that which minimises the sum of the squared masses of the mega-jet four-vectors. Using this mega-jet configuration a characteristic mass, M'_R, is defined in the rest frame of the sparticles (the so-called "R-frame"):

$$M'_R = \sqrt{(j_{1,E} + j_{2,E})^2 - (j_{1,L} + j_{2,L})^2},$$ (1)

where $j_{i,L}$ denotes the longitudinal momentum, and $j_{i,E}$ the energy in the R-frame, of the mega-jet i. The transverse information of the system is contained in another variable, M_T^R. In the di-sparticle decay there are two mega-jets, each with associated E_T^{miss} from the escaping LSPs. Assigning half of the missing transverse momentum per event to each of the LSPs, M_T^R is defined as

$$M_T^R = \sqrt{\frac{|\vec{E}_T^{\text{miss}}|(|\vec{j}_{1,\text{T}}| + |\vec{j}_{2,\text{T}}|) - \vec{E}_T^{\text{miss}} \cdot (\vec{j}_{1,\text{T}} + \vec{j}_{2,\text{T}})}{2}}, \qquad (2)$$

where $j_{i,T}$ denotes the transverse momentum of the mega-jet i.

Finally a Razor variable is defined:

$$R = \frac{M_T^R}{M_R'}. \qquad (3)$$

For SM processes R tends to have a low value, while it is approximately uniformly distributed between 0 and 1 for SUSY-like signal events. Thus R is a discriminant between signal and background. A selection using R is made to reduce background processes before a search for new physics is performed in the distribution of the variable M_R'.

Signal regions are defined to target two different regions of kinematic phase space characteristic of decays resulting from pair-produced squarks and gluinos. In order to define these kinematic regions the one-step gluino (squark) simplified models are used.

In models at high x (see Section 2.1) the mass difference between the gluino (squark) and chargino is at a minimum, and so a high-p_T W yields a high-p_T neutrino and a charged lepton. In addition, a heavier chargino relative to the gluino (squark) results in fewer high-p_T jets. This results in less observable mass in the event, and hence lower M_R'. The potential for large missing energy pointing away from the mega-jets gives rise to large M_T^R, and so R tends to take on larger values.

Different kinematics can be identified at lower x, where the mass splitting between the chargino and LSP is smaller, and hence more visible mass gives rise to higher M_R' and R is generally lower. The large mass difference between the gluino (squark) and chargino allows for higher p_T and more numerous jets.

These distinct regions of differing event kinematics motivate two different signal region selections, which are further separated into opposite- and same-lepton flavour channels. The first same- and opposite-flavour signal region (SR1) requires exactly two signal leptons satisfying all event selection and trigger requirements, and targets signal events with high-x-like topologies. The selection includes events with fewer than three jets with $p_\text{T} > 50$ GeV, $R > 0.5$ and $M_R' > 400$ GeV. The second of the signal region selections (SR2) targets events with low-x like topologies, requiring at least two jets ($p_\text{T} > 50$ GeV), $R > 0.35$ and $M_R' > 800$ GeV.

Each of these signal regions excludes events containing b-tagged jets, since heavy flavour decays are not expected in the simplified SUSY models interpreted in this analysis. In addition, in order to minimise the background due to leptonically decaying Z-bosons, a Z-veto is introduced in all same-flavour signal regions. The location of the signal regions in the R–M_R' plane is illustrated in Fig. 2. All four signal regions are orthogonal to one another, enabling the combination of the results from each. To produce model independent upper limits on the visible BSM production cross section (σ_{BSM}) and the number of BSM events (N_{BSM}), the signal regions are analysed one at a time and are each constructed as a single bin in M_R', so as to avoid including any information on the shape of the signal distribution. To provide stringent limits for models with larger mass splittings and low jet multiplicities, two discovery regions (DRs) are defined. The $ee/\mu\mu$ and $e\mu$ discovery regions have identical selections to those of their respective SR1 counter-parts, but the lower M_R' threshold is raised to 600 GeV. Full details of the signal region and discovery region selection criteria can be found in Table 3.

4 Background Estimation

In order to establish an observation of physics beyond the Standard Model in any of the signal regions, a reliable prediction of the SM backgrounds in these regions is necessary. The $t\bar{t}$ and $Z + X$ backgrounds

	b-jets	Z-veto	N_{Jets}	Jet p_{T}	R Range	M'_R Range [GeV]	M'_R bins
Signal Regions							
$ee/\mu\mu$ SR 1	No	Yes	≤ 2	> 50	$R > 0.5$	$400 < M'_R$	8
$e\mu$ SR 1	No	No	≤ 2	> 50	$R > 0.5$	$400 < M'_R$	8
$ee/\mu\mu$ SR 2	No	Yes	≥ 3	> 50	$R > 0.35$	$800 < M'_R$	5
$e\mu$ SR 2	No	No	≥ 3	> 50	$R > 0.35$	$800 < M'_R$	5
Discovery Regions							
$ee/\mu\mu$ DR	No	Yes	≤ 2	> 50	$R > 0.5$	$600 < M'_R$	1
$e\mu$ DR	No	No	≤ 2	> 50	$R > 0.5$	$600 < M'_R$	1
Control Regions							
$ee/\mu\mu$ Z CR 1	No	Yes	≤ 2	> 50	$0.15 < R < 0.3$	$400 < M'_R < 1200$	8
$ee/\mu\mu$ Z CR 2	No	Yes	≥ 3	> 50	$0.05 < R < 0.2$	$800 < M'_R < 1600$	4
$ee/\mu\mu$ Top CR 1	Yes	Yes	≤ 2	> 50	$0.2 < R < 0.4$	$400 < M'_R < 1200$	8
$e\mu$ Top CR 1	Yes	No	≤ 2	> 50	$0.2 < R < 0.4$	$400 < M'_R < 1200$	8
$ee/\mu\mu$ Top CR 2	Yes	Yes	≥ 3	> 50	$0.1 < R < 0.3$	$800 < M'_R < 1600$	4
$e\mu$ Top CR 2	Yes	No	≥ 3	> 50	$0.1 < R < 0.3$	$800 < M'_R < 1600$	4
Validation Regions							
$ee/\mu\mu$ Z VR 1	No	Yes	≤ 2	> 50	$0.25 < R < 1$	$200 < M'_R < 400$	4
$ee/\mu\mu$ Z VR 2	No	Yes	≥ 3	> 50	$0.1 < R < 1$	$200 < M'_R < 800$	6
$ee/\mu\mu$ Top VR 1	Yes	Yes	≤ 2	> 50	$0.5 < R < 1$	$200 < M'_R < 400$	4
$e\mu$ Top VR 1	Yes	No	≤ 2	> 50	$0.5 < R < 1$	$200 < M'_R < 400$	4
$ee/\mu\mu$ Top VR 2	Yes	Yes	≥ 3	> 50	$0.35 < R < 1$	$200 < M'_R < 800$	6
$e\mu$ Top VR 2	Yes	No	≥ 3	> 50	$0.35 < R < 1$	$200 < M'_R < 800$	6

Table 3: Control, validation and signal region definitions. The validation regions are not used to constrain the fit, but the M'_R-binning in these regions is included for completeness.

are estimated using dedicated control regions, wherein the MC simulation is normalised to the data. The background from mis-identified leptons is estimated using a data-driven approach. Additional irreducible or small backgrounds are estimated directly using MC simulation. A simultaneous fit, binned in M'_R, is performed in the control regions. The results of this fit are then used to estimate the background contribution to the signal regions (see Section 6).

4.1 $t\bar{t}$ and Z+jets Background

The primary backgrounds for the high-multiplicity two-lepton signal selection are those due to fully-leptonic $t\bar{t}$ and, to a much lesser extent, Z/γ^*+jets, where the Z-boson decays leptonically. These backgrounds are estimated using control regions defined such that they are enriched with events from the relevant SM process. The normalisation of the simulated $t\bar{t}$ or Z/γ^*+jets events is adjusted according to a binned fit to data in M'_R in these control regions.

In order to estimate the background due to these SM processes in a control sample with signal-like selection cuts, a control region catering to each signal region is defined. The top quark production and Z/γ^*+jets production control regions (Top CRs and Z CRs) are constructed using the same lower M'_R and jet multiplicity requirements as the signal region. The Z-mass veto is also kept in place for the same-flavour channels, in an attempt to keep the control region environment as similar to the signal regions as possible. As a result, the Z/γ^*+jets control region is dominated by the production of di-leptons with low mass. The Z control regions are also used to estimate the background due to WZ and ZZ diboson production. In the same-flavour channels the total $Z + X$ background is generally composed of ~ 70 % Z/γ^*+jets and 30 % WZ diboson events. Since few leptonically decaying Z-bosons are expected in the $e\mu$-channel, the Z control regions are defined for the same-flavour lepton channels only. In the $e\mu$-
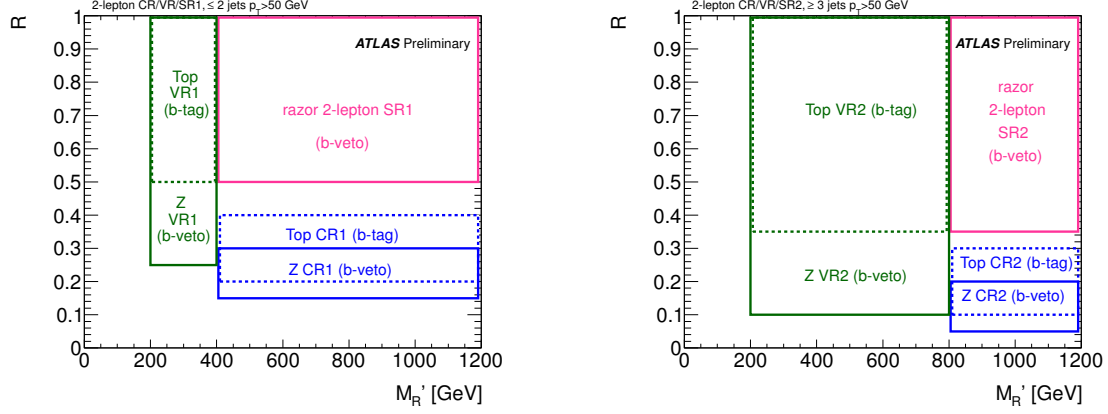
Figure 2: The low jet (left) and high jet (right) multiplicity control, validation, and signal regions in the M_R'–R plane.

channel, the (small) Z background is estimated directly from MC simulation and, in the signal region, mostly results from WZ diboson processes.

For the Z/γ^*+jets control region corresponding to SR1, the upper R-cut is lowered to 0.3, with a lower threshold of 0.15. This isolates the background due to Z/γ^*+jets, which tends to populate the low-R regions, while cutting out the very low R region rich in mis-identified leptons. The top control region is defined in the R-range $0.2 < R < 0.4$, and a requirement of at least one b-tagged jet is imposed in order to make this region completely orthogonal to the Z/γ^*+jets control sample, which employs a b-veto to mimic the signal regions. In the case of SR2, the Z/γ^*+jets control region is constructed to include the R-range $0.05 < R < 0.35$, while the top control region has $0.1 < R < 0.3$. Both control regions retain the jet-multiplicity cuts of SR2, as well as the Z-veto (with the exception of the $e\mu$ top control region, which has no veto on the Z-mass window). The b-jet requirements for these high jet multiplicity top and Z control regions are the same as their SR1 counterparts. The control region selection criteria are summarised in Table 3 and illustrated in Fig. 2. The R and M_R' distributions are shown, for the Z control regions in Fig. 3-4 and for the top control regions in Fig. 5-8. These distributions are made following the fit to the SM backgrounds (described in Section 6) in these regions. The systematic uncertainties, discussed in Section 5, are indicated as hatched lines.

4.2 Misidentified-lepton Background

The background due to semi-leptonic $t\bar{t}$ and W+jets enters into the two-lepton signal regions with jets being mis-identified as leptons, or with a real lepton from a heavy-flavour decay being sufficiently isolated to pass the signal lepton requirements. The background due to lepton mis-identification is estimated using a matrix method applied to non-isolated leptons in data. In this sample the number of events in which a mis-identified lepton passes signal-like requirements is estimated using the identification efficiency for real leptons and the efficiency for rejecting mis-identified leptons in data. The real lepton identification efficiency is estimated as a function of lepton p_T and η from leptonic Z-boson decays in data and cross-checked with simulation. Efficiencies for mis-identified lepton rejection are estimated in a data control sample enriched with multi-jet events, as described in Ref. [18]. Multi-jet control samples are separated according to the presence or absence of a b-tagged jet, so as to distinguish between heavy-flavour leptons passing signal lepton criteria and light jets being mis-identified as leptons.
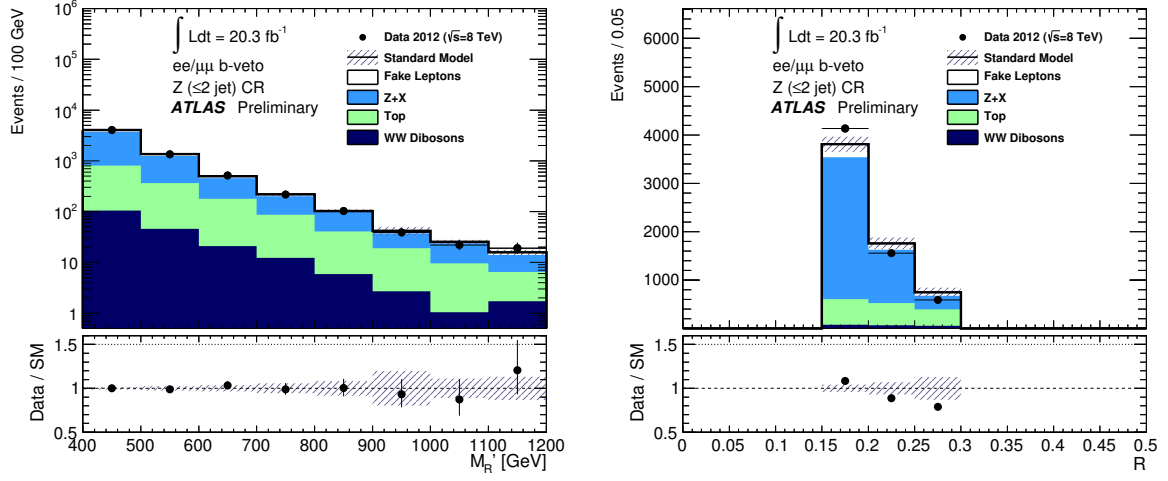
Figure 3: The distribution in M'_R (left) and R (right) after the fit to the Standard Model backgrounds in the control regions described in Section 6 in the same-flavour channels in the low jet multiplicity Z control region (Z CR1). For each distribution data to SM prediction ratios are also shown. Statistical and systematic uncertainties are indicated.
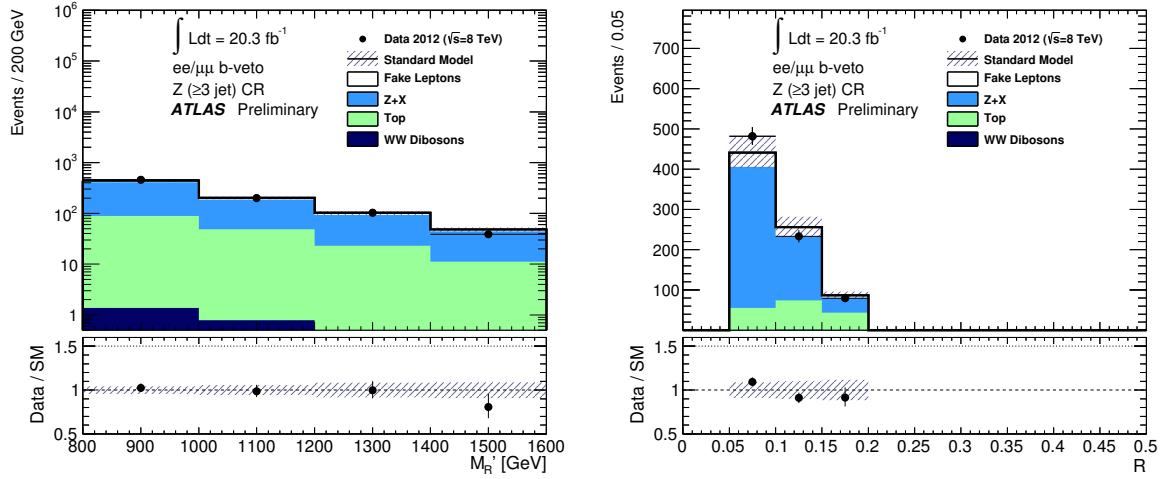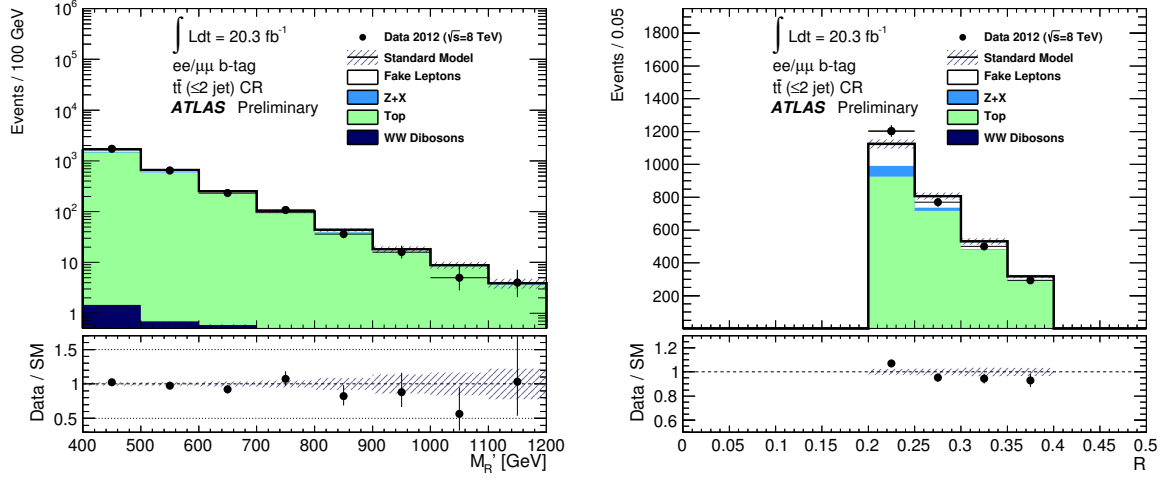

Figure 4: The distribution in M'_R (left) and R (right) after the fit to the Standard Model backgrounds in the control regions described in Section 6 in the same-flavour channels in the high jet multiplicity Z control region (Z CR2). For each distribution data to SM prediction ratios are also shown. Statistical and systematic uncertainties are indicated.
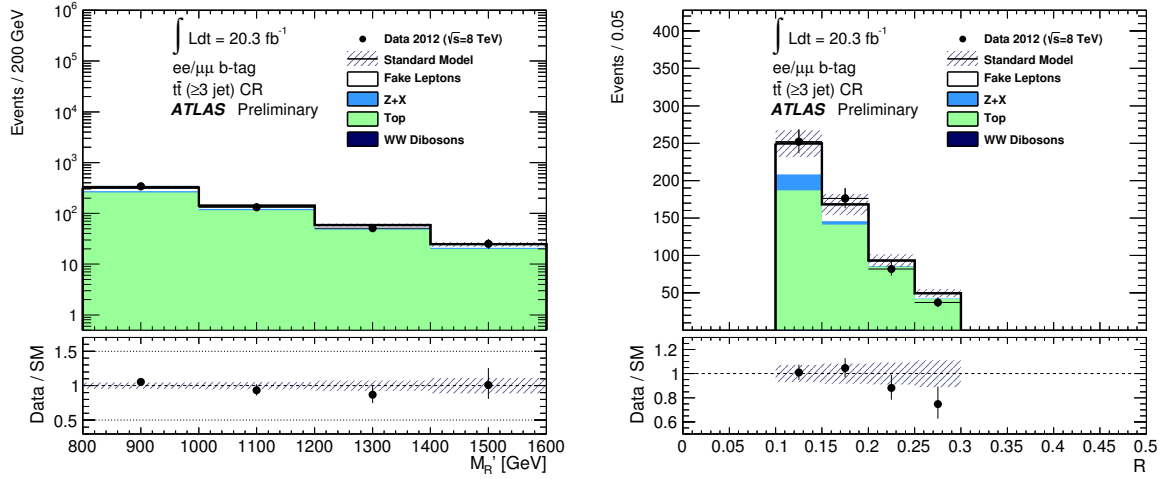
Figure 5: The distribution in M'_R (left) and R (right) after the fit to the Standard Model backgrounds in the control regions described in Section 6 in the same-flavour channels in the low jet multiplicity top control region (Top CR1). For each distribution data to SM prediction ratios are also shown. Statistical and systematic uncertainties are indicated.

Figure 6: The distribution in M'_R (left) and R (right) after the fit to the Standard Model backgrounds in the control regions described in Section 6 in the same-flavour channels in the high jet multiplicity top control region (Top CR2). For each distribution data to SM prediction ratios are also shown. Statistical and systematic uncertainties are indicated.
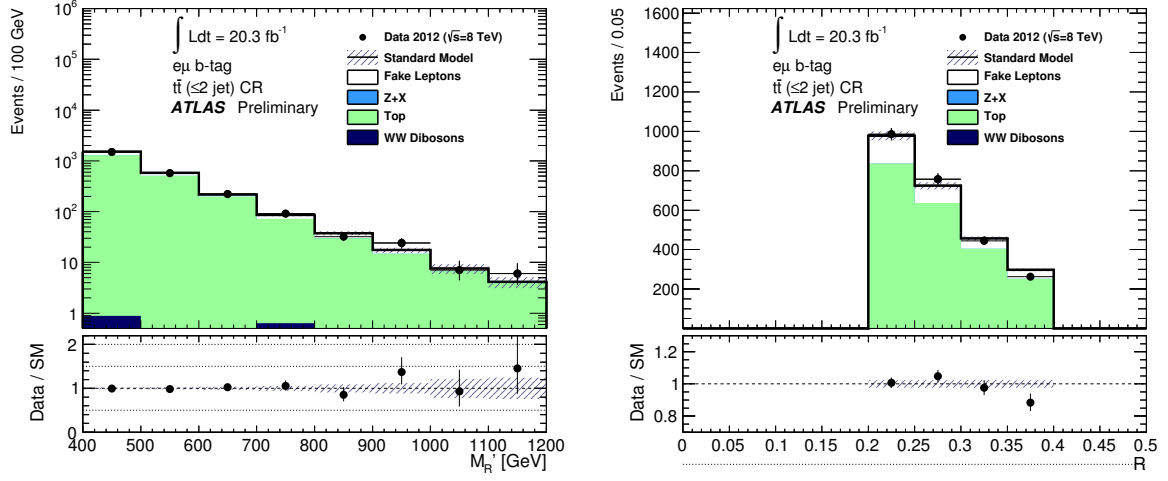
Figure 7: The distribution in M'_R (left) and R (right) after the fit to the Standard Model backgrounds in the control regions described in Section 6 in the electron-muon channel in the low jet multiplicity top control region (Top CR1). For each distribution data to SM prediction ratios are also shown. Statistical and systematic uncertainties are indicated.
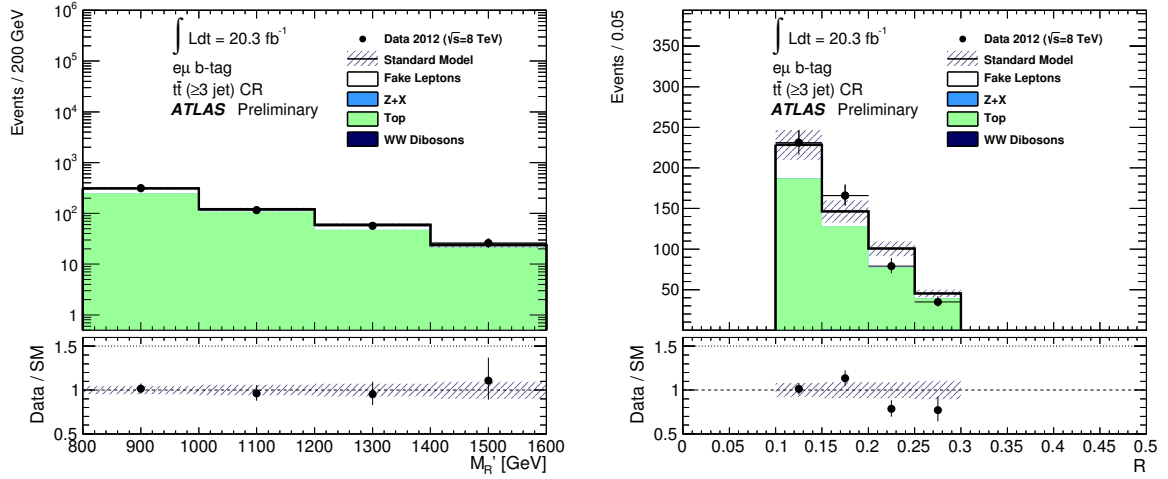

Figure 8: The distribution in M'_R (left) and R (right) after the fit to the Standard Model backgrounds in the control regions described in Section 6 in the electron-muon channel in the high jet multiplicity top control region (Top CR2). For each distribution data to SM prediction ratios are also shown. Statistical and systematic uncertainties are indicated.

4.3 Other Backgrounds

The largest remaining background in the low-multiplicity regions, the *WW* diboson background, is estimated entirely from simulation. The single top production and $t\bar{t}+V$ production backgrounds are constrained using the top control regions, where the $t\bar{t}$, single top and $t\bar{t}+V$ production backgrounds are treated as one correlated background. This is motivated by the fact that all top production processes present a similar shape in M'_R and differ only in terms of normalisation. In this top sample, $t\bar{t}$ production typically comprises 90-95 % of the sample, with $t\bar{t}+V$ providing 1 % and single top production making up the remaining 4-9 %.

5 Systematic Uncertainties

The systematic uncertainties associated with the various aspects of the estimation of the SM backgrounds in the signal regions impact the predicted event yields. The uncertainties considered in this analysis can be separated into two categories: experimental uncertainties and theoretical uncertainties.

The experimental uncertainties accounted for include those on the jet energy scale, which are derived from a combination of test-beam measurements and cross-checks using simulation. In addition, in situ studies in *pp* collisions at ATLAS are used to measure the jet energy scale uncertainties [71, 72], as well as the uncertainty on the jet energy resolution [73]. The uncertainties associated with the tagging of *b*-jets include the uncertainty on the *b*-tagging efficiency [74] and the mis-tag rates for light- and charm-quarks [75] (the probability that a *b*-tagged jet does not contain a heavy flavour decay). The dominant experimental uncertainties in the analysis are those from the jet energy scale (typically 5-15 %) and *b*-tagging (typically 10-15 %).

An uncertainty is assigned to the JVF requirement on jets between $30 < p_T < 50$ GeV, by varying the JVF threshold up and down by 0.05. Uncertainties on the soft energy scale and resolution are applied to the E_T^{miss}. In the case of the mis-identified lepton background, the statistical uncertainty on the number of events in the control samples is taken into account, as well as an uncertainty on the real lepton identification efficiency and on the subtraction of other real lepton backgrounds from the control samples used to estimate the lepton mis-identification efficiency. A 5 % uncertainty is applied to the trigger efficiency based on studies comparing efficiencies in data and Monte Carlo [76]. Small uncertainties ($\sim$2 %) due to differences in lepton reconstruction and identification efficiencies between data and MC simulation are taken into account. Uncertainties on lepton momentum scales and resolutions are found to be negligible.

Several sources of theoretical systematic uncertainties are taken into account. In the case of the $t\bar{t}$ background, variations of the renormalisation and factorisation scales and variations of the PDFs are considered. In addition, uncertainties on the parton shower modelling are derived from comparing POWHEG+PYTHIA and POWHEG+JIMMY samples. Variations in initial and final state radiation (ISR/FSR), estimated using AcerMC generated samples with different tunes, are also accounted for.

The single top production and $t\bar{t}+V$ production backgrounds have a fixed relative normalisation with respect to the $t\bar{t}$ production sample. In the case of single top production an additional systematic uncertainty is derived from the difference between the nominal MC@NLO single top sample and POWHEG samples showered with both PYTHIA and HERWIG/JIMMY, and using either the diagram removal or diagram subtraction [77] scheme to estimate interference effects in the single top production diagrams.

For the *Z*+jets background variations of the renormalisation and factorisation scales are taken into account, as are variations in PDFs. An additional uncertainty is applied based on the difference between Z/γ^* samples generated with up to four and up to five jets in the matrix element.

The *WW* diboson background is assigned a 5 % cross section uncertainty, while the normalisation of the other diboson samples are correlated with the *Z*+jets sample. Systematic uncertainties due to the MC modelling are assessed by comparing the nominal estimates with two alternative generators.

The differences between the nominal Powheg diboson samples and aMC@NLO [78] generated samples are used to account for scale variation and generator cutoff uncertainties. The differences between the nominal Powheg diboson sample and one generated with Sherpa are used to account for the effect of additional partons in the matrix element. These modelling uncertainties are typically ∼ 25 %.

For the signal models, theoretical uncertainties on the acceptance are assessed. The modelling of ISR plays an important role for scenarios in which there are small mass differences in the heavy sparticle decay cascade. Uncertainties are derived by varying the following parameters in the MadGraph5+Pythia generated samples up and down by a factor of two [79]: the scale used to determine the event-by-event renormalisation and factorisation scale, the QCD radiation scale parameter, the parameter controlling the Λ_{QCD} value used for FSR (this parameter is scaled by 0.5 and 1.5) and the MadGraph parameter used for jet matching. The uncertainties are negligible for a mass difference between the produced sparticle and the LSP above 300 GeV, and they reach 38 % for the lowest squark masses and smallest mass splittings considered.

A 2.8 % uncertainty on the luminosity determination is included for all signal and background MC simulation samples. The uncertainty is derived, following the same methodology as that detailed in Ref. [80], from a preliminary calibration of the luminosity scale derived from beam-separation scans performed in November 2012.

6 Background Fit

The expected event yields in the signal regions due to background processes are estimated using a profile likelihood [81] fit, applied simultaneously over the control regions, which are binned in M'_R, as described in Section 4 and summarised in Table 3. During the fit in the control regions it is assumed that there is no signal contamination present. Correlations from sample-to-sample between each of the fitted regions are taken into account, and the systematic uncertainties from the same source are correlated over all regions. The normalisations of those backgrounds that are not estimated in control regions are constrained using estimates derived either from simulation or data driven techniques. The normalisation of the top quark production and Z production backgrounds is allowed to differ between control regions, in order to allow for small differences in kinematics (e.g. differences due to the different minimum lepton p_T threshold). The fit setup can be imagined to consist of four "slices." Each slice comprises a single lepton flavour combination and jet-multiplicity, so that each SR is associated with a CR that has the same lepton flavour and jet-multiplicity requirements. Each slice shares a common normalisation parameter on the top quark production and Z production background. All statistical and systematic uncertainties are treated as nuisance parameters in the fit, as described in Ref. [18]. The shape and normalisation of the backgrounds may be modified in the fit based on the variations allowed by the systematic uncertainties. These changes are propagated onto the background prediction in the signal region. Several distinct background components are included in the fit:

- **Top background:** This includes $t\bar{t}$, single top and $t\bar{t}+V$ production processes. Simulation is normalised to data in dedicated control regions. The results of the background fit in the control regions are extrapolated to the corresponding signal regions using MC simulation.

- **$Z + X$ background:** This includes Z/γ^*+jets, WZ and ZZ diboson processes. The treatment here is the same as the treatment of the top quark production background above: the Z/γ^*+jets, WZ and ZZ diboson production processes are treated with a common normalisation factor.

- **WW diboson background:** The number of events in the signal region is predicted from simulation. The fit is permitted to vary the normalisation within a 5 % NLO cross section uncertainty.

channel	Z CR 1	Z CR2
Observed events	6283	794
Fitted bkg events	6282 ± 80	795 ± 28
Fitted DibosonWW events	196 ± 35	3 ± 3
Fitted ZX events	4298 ± 250	558 ± 50
Fitted Top events	1315 ± 220	169 ± 34
Fitted reducible bkg. events	474 ± 110	65 ± 24
MC exp. SM events	7029	901
MC exp. DibosonWW events	189	4
MC exp. ZX events	5089	630
MC exp. Top events	1279	193
Exp. reducible bkg. events	471	74

Table 4: Background fit results for the Z control regions, for an integrated luminosity of 20.3 fb^{-1}. Nominal MC expectations (normalised to MC cross-sections) are given for comparison. The errors shown are the statistical plus systematic uncertainties.

For this background, there are also substantial ($\sim$ 25 %) theoretical uncertainties that enter the fit. The result of the fit in the control regions is extrapolated to the signal regions.

- **Mis-identified lepton background:** The event yield in each region is predicted using the number of events obtained using the data driven matrix method. Each region is considered independent and is allowed to vary within the uncertainties of the prediction.

The results of the background fit to the control regions are tested in validation regions (VR), to cross-check the validity of the control region to signal region extrapolation. Each control and signal region has a dedicated validation region, which is used to provide a data-to-prediction comparison and does not constrain the fit. The validation regions are summarised, along with the control and signal regions, in Table 3.

The contribution of each background to each of the control regions before and after the fit are shown in Tables 4 and 5. The before-fit simulation predictions are generally close to the fitted values. The uncertainties shown are only the uncertainties on the total yield in each region. There are significant uncertainties affecting the shapes of the distributions, which do not affect the integrated number of expected events. In addition, residual anti-correlations between the normalisations of the background components result in a smaller uncertainty on the total than on some of the individual backgrounds. After the fit, the dominant experimental uncertainties on the total yields are the normalisation uncertainty on $t\bar{t}$ (typically 10 %), the uncertainty on the b-tagging efficiency (10-15 %), and the jet energy scale (5-10 %).

The pre- and post-fit yields in the validation regions are displayed in Tables 6 and 7. Following the fit to the SM backgrounds in the control regions and subsequent extrapolation to the validation regions, the agreement in the VR yields is noticeably improved. In the validation regions the yields and shapes show good agreement with the Standard Model expectation. The after-fit R and M'_R distributions in the validation regions are shown in Fig. 9-14. Good agreement is obtained in all regions and the yields of all validation regions are within about 1σ of the prediction. This is shown in Fig. 15.

channel	Top $ee/\mu\mu$ CR1	Top $e\mu$ CR1	Top $ee/\mu\mu$ CR2	Top $e\mu$ CR2
Observed events	2766	2451	547	511
Fitted bkg events	2766 ± 70	2452 ± 50	546 ± 25	511 ± 23
Fitted DibosonWW events	3^{+5}_{-3}	2^{+4}_{-2}	$0.1^{+0.6}_{-0.1}$	$0.2^{+0.7}_{-0.2}$
Fitted ZX events	89 ± 50	0.87 ± 0.30	27 ± 9	0.18 ± 0.07
Fitted Top events	2405 ± 120	2124 ± 80	442 ± 40	422 ± 33
Fitted reducible bkg. events	269 ± 70	324 ± 70	78 ± 22	88 ± 24
MC exp. SM events	2819	2380	649	546
MC exp. DibosonWW events	5	4	0.3	0.4
MC exp. ZX events	61	0.62	24	0.16
MC exp. Top events	2407	2062	541	458
Exp. reducible bkg. events	346	313	84	87

Table 5: Background fit results for the top control regions, for an integrated luminosity of 20.3 fb^{-1}. Nominal MC expectations (normalised to MC cross-sections) are given for comparison. The errors shown are the statistical plus systematic uncertainties.

channel	Z VR1	Z VR2
Observed events	24956	3638
Fitted bkg events	23412 ± 1600	3567 ± 270
Fitted DibosonWW events	1161 ± 260	24 ± 5
Fitted ZX events	13352 ± 1600	2027 ± 240
Fitted Top events	6673 ± 1000	1039 ± 210
Fitted reducible bkg. events	2225 ± 500	477 ± 110
MC exp. SM events	25635	3992
MC exp. DibosonWW events	1087	24
MC exp. ZX events	15876	2327
MC exp. Top events	6446	1164
Exp. reducible bkg. events	2225	477

Table 6: Background fit results for the Z validation regions, for an integrated luminosity of 20.3 fb^{-1}. Nominal MC expectations (normalised to MC cross-sections) are given for comparison. The errors shown are the statistical plus systematic uncertainties.
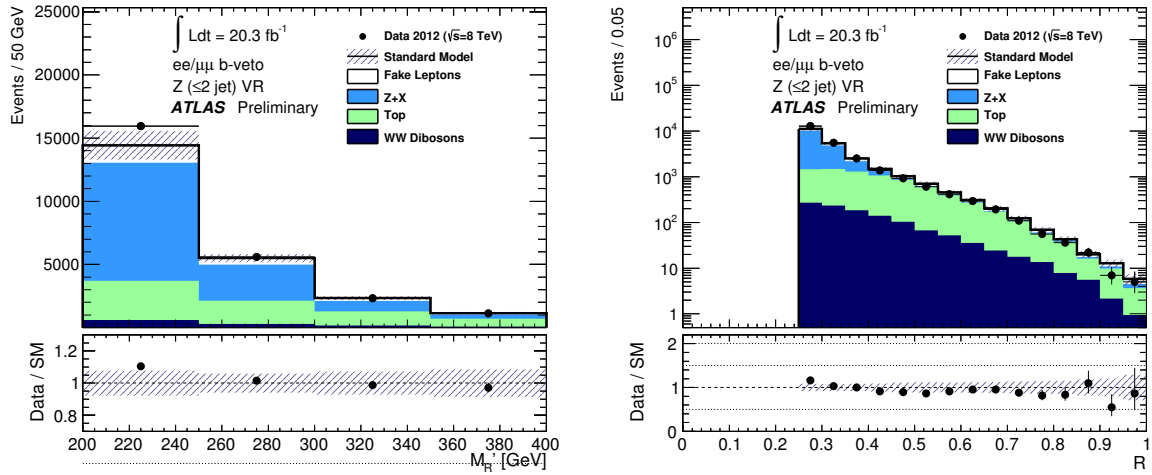
channel	Top $ee/\mu\mu$ VR1	Top $e\mu$ VR1	Top $ee/\mu\mu$ VR2	Top $e\mu$ VR2
Observed events	3064	2998	1112	1105
Fitted bkg events	2970 ± 150	2895 ± 130	1038 ± 100	1082 ± 110
Fitted DibosonWW events	2.8 ± 2.1	2.9 ± 2.7	0.6 ± 0.5	$0.3^{+0.8}_{-0.3}$
Fitted ZX events	2.8 ± 2.1	0.54 ± 0.07	$1.3^{+1.6}_{-1.3}$	0.16 ± 0.04
Fitted Top events	2575 ± 130	2539 ± 110	809 ± 90	849 ± 90
Fitted reducible bkg. events	389 ± 80	353 ± 70	227 ± 60	233 ± 60
MC exp. SM events	2904	2787	1170	1110
MC exp. DibosonWW events	3.6	4.1	0.8	0.3
MC exp. ZX events	1.6	0.54	0.7	0.14
MC exp. Top events	2510	2429	941	876
Exp. reducible bkg. events	389	353	227	233

Table 7: Background fit results for the top validation regions, for an integrated luminosity of 20.3 fb^{-1}. Nominal MC expectations (normalised to MC cross-sections) are given for comparison. The errors shown are the statistical plus systematic uncertainties.

Figure 9: The distribution in M'_R (left) and R (right) after the fit to the Standard Model backgrounds in the control regions (the results of which are extrapolated to the validation regions) described in Section 6 in the same-flavour channels in the low jet multiplicity Z validation region (Z VR1). For each distribution data to SM prediction ratios are also shown. Statistical and systematic uncertainties are indicated.
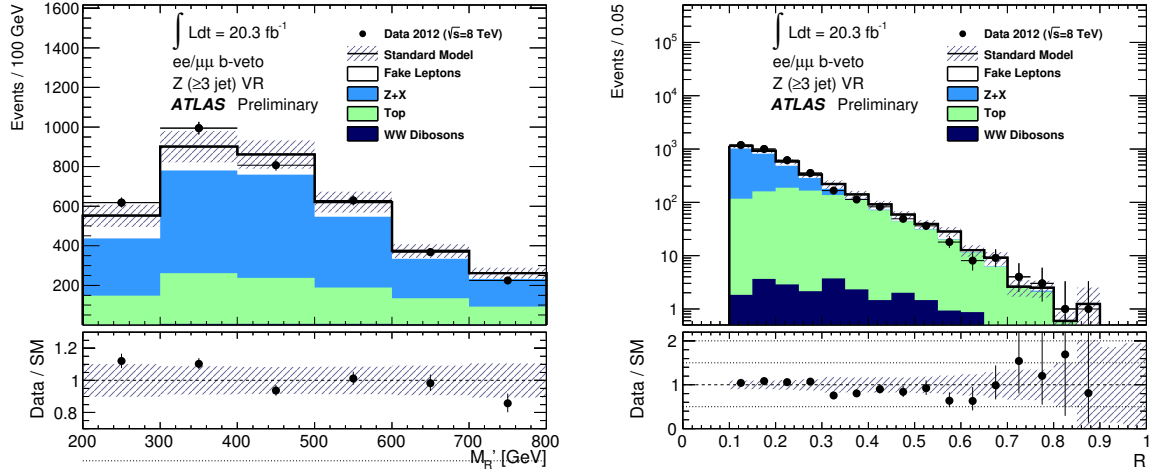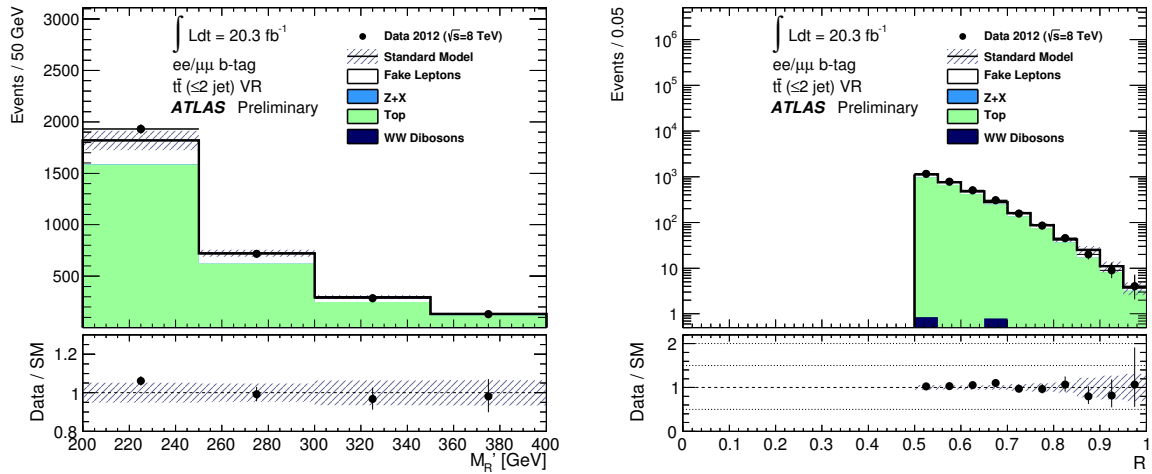
Figure 10: The distribution in M'_R (left) and R (right) after the fit to the Standard Model backgrounds in the control regions (the results of which are extrapolated to the validation regions) described in Section 6 in the same-flavour channels in the high jet multiplicity Z validation region (Z VR2). For each distribution data to SM prediction ratios are also shown. Statistical and systematic uncertainties are indicated.

Figure 11: The distribution in M'_R (left) and R (right) after the fit to the Standard Model backgrounds in the control regions (the results of which are extrapolated to the validation regions) described in Section 6 in the same-flavour channels in the low jet multiplicity top validation region (Top VR1). For each distribution data to SM prediction ratios are also shown. Statistical and systematic uncertainties are indicated.
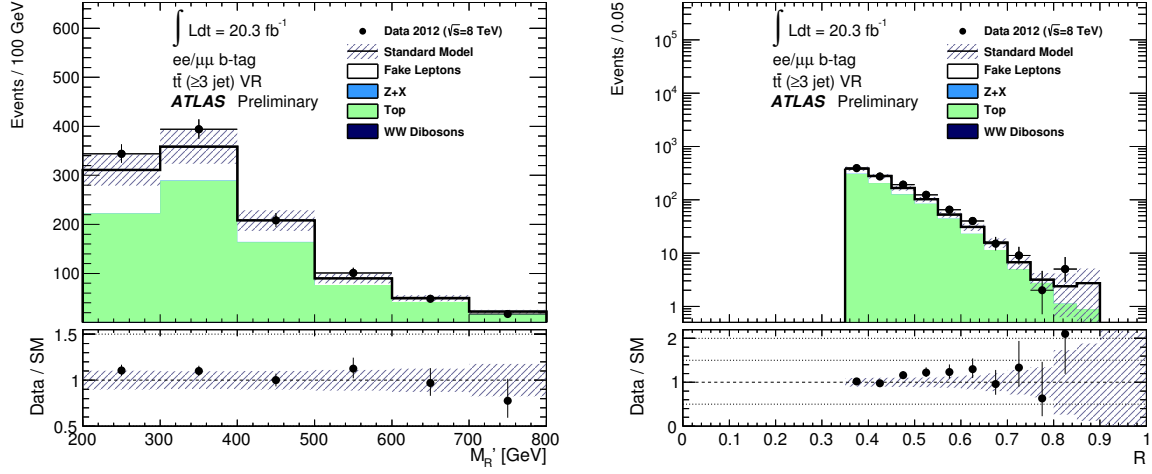
17

Figure 12: The distribution in M'_R (left) and R (right) after the fit to the Standard Model backgrounds in the control regions (the results of which are extrapolated to the validation regions) described in Section 6 in the same-flavour channels in the high jet multiplicity top validation region (Top VR2). For each distribution data to SM prediction ratios are also shown. Statistical and systematic uncertainties are indicated.
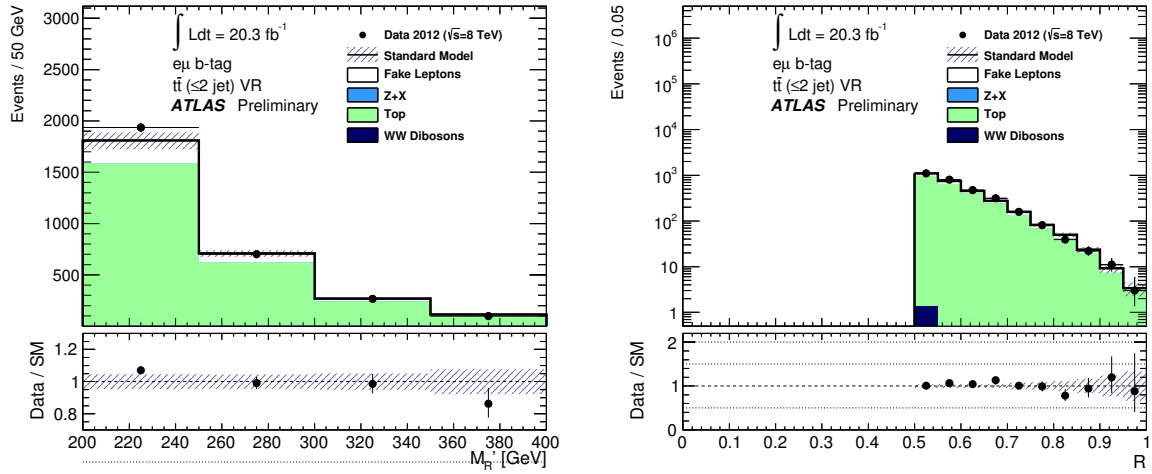

Figure 13: The distribution in M'_R (left) and R (right) after the fit to the Standard Model backgrounds in the control regions (the results of which are extrapolated to the validation regions) described in Section 6 in the electron-muon channel in the low jet multiplicity top validation region (Top VR1). For each distribution data to SM prediction ratios are also shown. Statistical and systematic uncertainties are indicated.

Figure 14: The distribution in M'_R (left) and R (right) after the fit to the Standard Model backgrounds in the control regions (the results of which are extrapolated to the validation regions) described in Section 6 in the electron-muon channel in the high jet multiplicity top validation region (Top VR2). For each distribution data to SM prediction ratios are also shown. Statistical and systematic uncertainties are indicated.
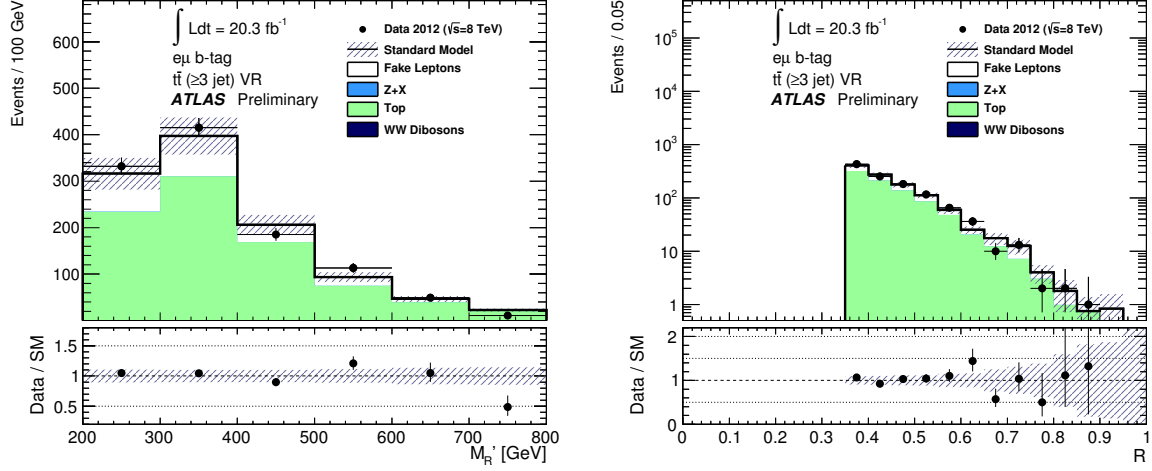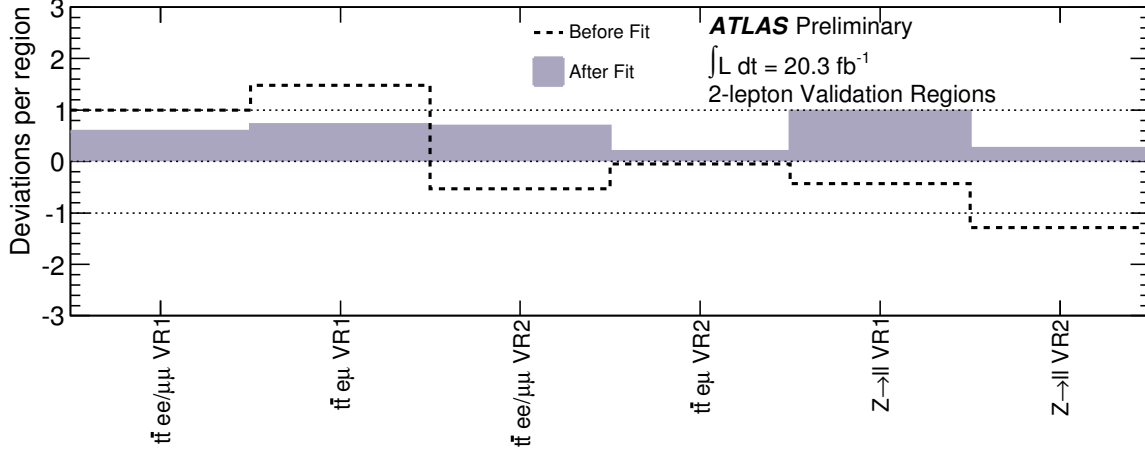

Figure 15: Summary of the agreement in the validation regions. This is shown in terms the number of observed minus the number of fitted events divided by the total statistical and systematic uncertainty of the prediction. The uncertainty after the fit is used. The dashed line shows the prediction before the fit and the shaded region the fitted background prediction.

7 Results and Interpretation

Tables 8 and 9 summarise the observed numbers of events in the signal regions and the predictions from the background fit to the control regions after extrapolation to the signal regions. No significant deviation from the expected backgrounds is observed in the data. The distributions of M'_R and R are shown in Figs. 16 and 17, respectively, where the arrows indicate the minimum requirements applied in the signal regions. The shaded bands exhibit the size of the total systematic uncertainty. Representative signal models are overlaid onto these distributions. In the low-multiplicity regions, two two-step decay signal models are included: one with gluino-gluino production, with masses of 705, 625, 585, and 545 GeV for the gluino, $\tilde{\chi}_1^\pm$ and $\tilde{\chi}_2^0$, sleptons and sneutrinos, and $\tilde{\chi}_1^0$, respectively, and one with gluino-gluino production, with masses of 465, 385, 345, and 350 GeV for the squarks, $\tilde{\chi}_1^\pm$ and $\tilde{\chi}_2^0$, sleptons and sneutrinos, and $\tilde{\chi}_1^0$, respectively. These models are chosen for their relatively low mass splittings and jet multiplicities. In the high-multiplicity regions, two different signal models are displayed: a one-step model with gluino-gluino production and masses of 800, 360, and 60 GeV for the gluino, $\tilde{\chi}_1^\pm$, and $\tilde{\chi}_1^0$, respectively, and a two-step model with gluino-gluino production and masses of 1105, 705, 505, and 305 GeV for the gluino, $\tilde{\chi}_1^\pm$ and $\tilde{\chi}_2^0$, sleptons and sneutrinos, and $\tilde{\chi}_1^0$, respectively. These models are chosen for their relatively high mass splitting and jet multiplicity.

Upper limits at the 95 % confidence level (CL) on the number of events from beyond the Standard Model processes in each of the signal regions are calculated using the CL_S method [82]. To make the upper limits model-independent, they are calculated using only one signal region at a time and without any signal region shape information. The limits are shown in Tables 8 and 9. They are also converted into upper limits on the visible cross section of BSM processes by dividing N_{BSM} by the integrated luminosity of the dataset. For evaluating consistency with the Standard Model expectation, p-values and Gaussian significances are also provided for each of these regions, again disregarding any shape information in the signal region.

The model-independent upper limits for the low-multiplicity signal regions are considerably weaker than those of the high-multiplicity signal regions, predominantly because they include low-mass, high-statistics bins to ensure sensitivity for SUSY models characterised by small mass splittings. To provide more stringent limits on models with larger mass splitting, two discovery regions, $ee/\mu\mu$ and $e\mu$ DR, are constructed with a higher M'_R requirement of $M'_R > 600$ GeV (c.f. the signal regions' standard cut of $M'_R > 400$ GeV). The model independent limits for these regions are presented in Table 10 and 11. These limits and the corresponding p-values are, of course, highly correlated with those in the previous tables.

Several SUSY-inspired simplified models are used for the interpretation of the fit results. A binned likelihood fit is performed considering simultaneously both the signal and control regions, again using the CL_S method to determine whether a signal model is excluded at 95 % CL. The fit, binned in M'_R, is performed for each point in parameter space, and it thus takes into account any signal contamination in the control regions.

Limits for the various models are shown in Fig. 18–21. In these figures, the yellow band around the expected limit shows the $\pm 1\sigma$ uncertainty region including all statistical and systematic uncertainties except the theoretical uncertainties on the model's production cross section. The dotted theoretical uncertainty lines around the observed limit are obtained by changing the production cross section by $\pm 1\sigma$. All mass limits of supersymmetric particles quoted later in this section are derived from the -1σ SUSY theory line. Although the number of observed events is somewhat smaller than the number of expected events in these signal regions, the observed limit is not consistently stronger than the expected. This results from the bin-by-bin fluctuations of the data around the expectation and the variation of the distribution of signal events across each model's parameter space.

The limits for a model with gluino pair production, where the gluinos decay through a chargino to the LSP, are shown in Fig. 18. Similar models with light squark pair production, where the squarks decay
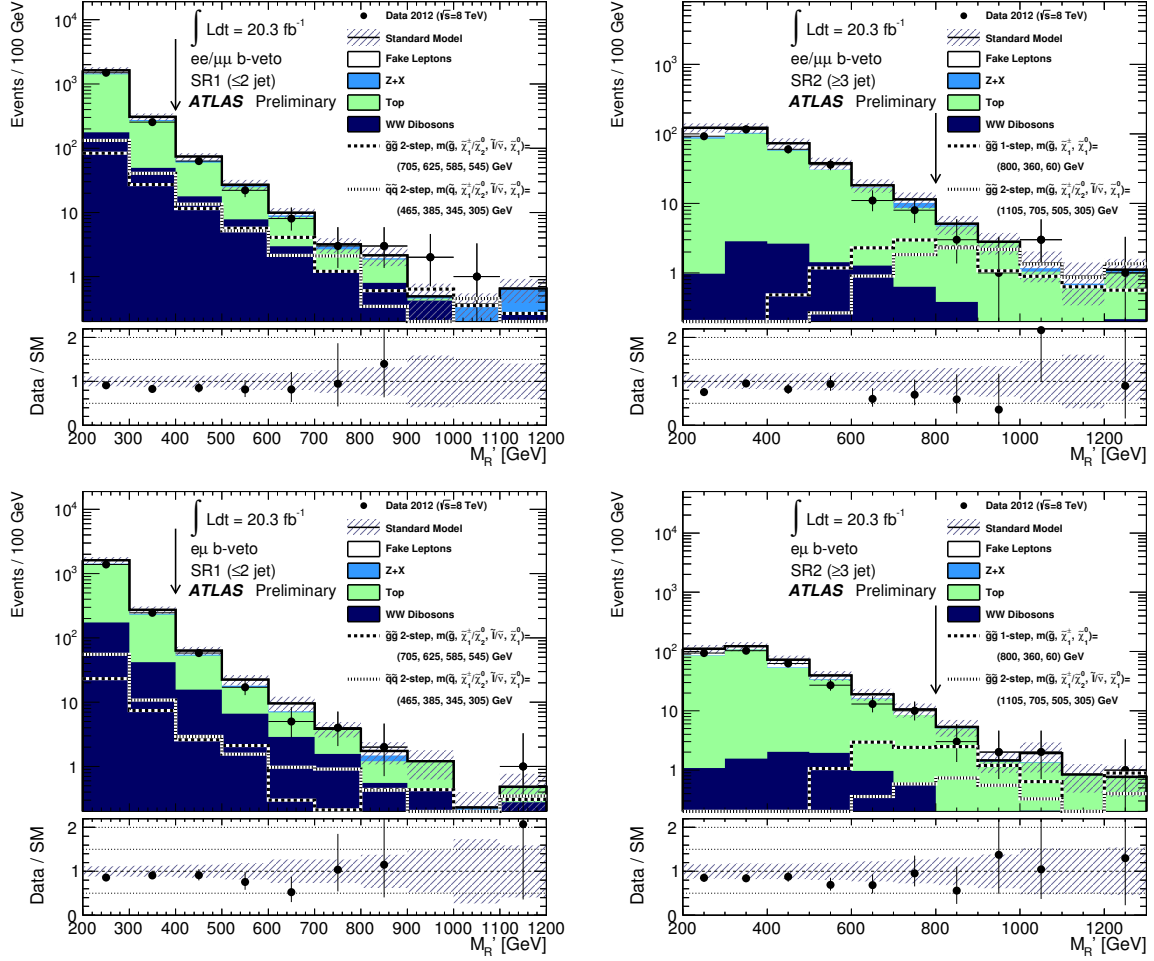
Figure 16: The distribution in M'_R in the low jet multiplicity SR1 (left) and high jet multiplicity SR2 (right), with all requirements except that on the minimum M'_R applied, in the same-flavour (top) and opposite-flavour (bottom) channels. For each distribution data to SM prediction ratios are also shown. Statistical and systematic uncertainties are indicated. Two representative signal distributions are overlaid. The lower signal region bounds in M'_R are indicated with arrows.

through a chargino to the LSP, are shown in Fig. 19. Because of the significantly higher production cross section, the limits on the gluino simplified models are considerably stronger. At low x, the Razor variables in the di-lepton channel provide strong limits compared to other channels, excluding gluinos with masses up to 820 GeV and squarks with masses up to 500 GeV. For a light LSP, gluinos with masses below 760 GeV and squarks with masses below 450 GeV are excluded. The limits of the SUSY search in events with one lepton from Ref. [18], overlaid in Fig. 19, are stronger at moderate and high x. The leptons in these models come exclusively from W decays, leading to a lower visible cross section and weaker limits in general for this analysis. The additional reach is largely due to the sensitivity to softer leptons and to the lack of an explicit $E_{\mathrm{T}}^{\mathrm{miss}}$ cut in this analysis. The minimal M'_R requirement in the signal region harms the limit in the small mass splitting region relative to the soft lepton analysis described in Ref. [18]. The low-x limits in the squark-squark model suffer from large MC simulation statistical uncertainties.

The limits for models with either gluino or squark pair-production, where the gluino or squark decays in two steps through a chargino and then through either a slepton or sneutrino to the LSP, are shown in
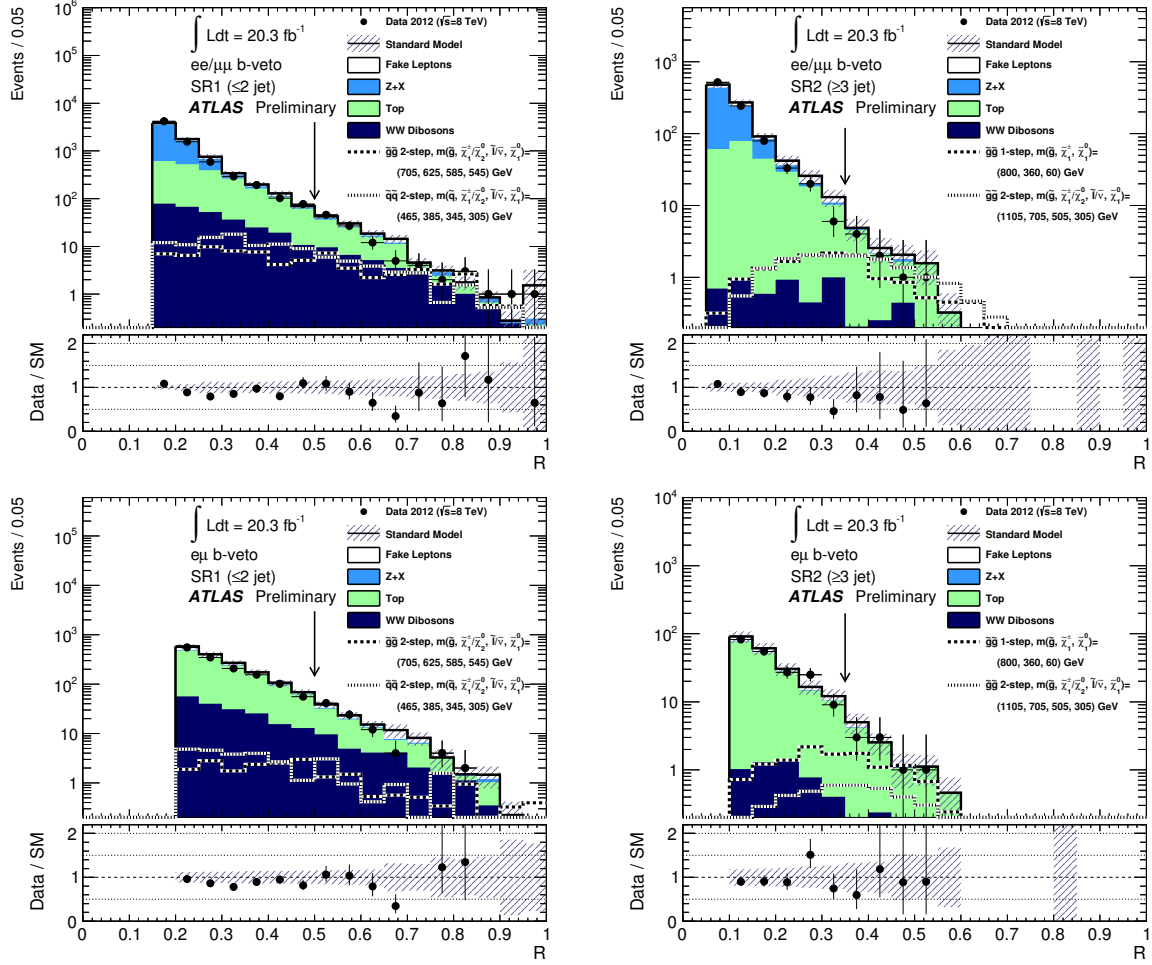
Figure 17: The distribution in R in the low jet multiplicity SR1 (left) and high jet multiplicity SR2 (right), with all requirements except that on the minimum R applied, in the same-flavour (top) and opposite-flavour (bottom) channels. For each distribution data to SM prediction ratios are also shown. Statistical and systematic uncertainties are indicated. Two representative signal distributions are overlaid. The lower signal region bounds in R are indicated with arrows.

Fig. 20. Again, the significant difference in production cross section results in a much stronger limit in the gluino case than in the squark case. The limits from Ref. [18] are also overlaid in these figures. For a light LSP, gluinos with masses below 1120 GeV and squarks with masses below 740 GeV are excluded. In this model, because the leptons can come from several different decay points, a high fraction of events contain two leptons, making the limits in this model some of the strongest of any ATLAS analysis to date. In particular, the fractions of events with exactly one and exactly two leptons are comparable over most of the parameter space of this model.

The limits for the minimal universal extra dimensions model are shown in Fig. 21. As the cross sections for this model are calculated at leading order with HERWIG++, no theoretical uncertainty on the production cross section is shown. At low ΛR_c, the signal region acceptance drops because of the minimum M'_R requirement. The high ΛR_c, the limit set by this analysis reaches 870 GeV in $1/R_c$, exceeding that of Ref. [18] thanks to the higher sensitivity to models with large mass splitting.

channel	$ee/\mu\mu$ SR1	$e\mu$ SR1	$ee/\mu\mu$ SR2	$e\mu$ SR2
Observed events	102	87	8	8
Fitted bkg events	117 ± 16	103 ± 15	11.0 ± 2.8	10.1 ± 2.7
Fitted DibosonWW events	32 ± 8	28 ± 7	0.9 ± 0.3	0.44 ± 0.15
Fitted ZX events	6.8 ± 1.5	3.6 ± 0.3	0.57 ± 0.14	0.22 ± 0.06
Fitted Top events	66 ± 11	55 ± 10	8.9 ± 2.4	8.6 ± 2.4
Fitted reducible bkg. events	13 ± 7	16 ± 8	$0.7^{+1.0}_{-0.7}$	$0.8^{+1.1}_{-0.8}$
MC exp. SM events	115	101	12.8	10.4
MC exp. DibosonWW events	29	26	0.8	0.50
MC exp. ZX events	8.2	3.5	0.70	0.19
MC exp. Top events	65	56	10.6	8.9
Exp. reducible bkg events	13	16	0.7	0.8
95 % C.L. upper limit on N_{BSM}	$28\ (35^{\uparrow 48}_{\downarrow 25})$	$24\ (31^{\uparrow 43}_{\downarrow 23})$	$6.7\ (8.5^{\uparrow 12.4}_{\downarrow 6.0})$	$7.1\ (8.4^{\uparrow 12.2}_{\downarrow 5.9})$
95 % C.L. upper limit on σ_{BSM} [fb]	$1.4\ (1.7^{\uparrow 2.3}_{\downarrow 1.2})$	$1.2\ (1.5^{\uparrow 2.1}_{\downarrow 1.1})$	$0.33\ (0.42^{\uparrow 0.61}_{\downarrow 0.29})$	$0.35\ (0.41^{\uparrow 0.60}_{\downarrow 0.29})$
p_0-value (Gauss. σ)	$0.76\ (-0.70)$	$0.80\ (-0.86)$	$0.77\ (-0.75)$	$0.69\ (-0.49)$

Table 8: Observed numbers of events and predictions from the fit to the SM backgrounds in the control regions extrapolated to the signal regions, for an integrated luminosity of 20.3 fb^{-1}. Nominal MC expectations (normalised to MC cross sections) are given for comparison. The errors shown are the statistical plus systematic uncertainties. The observed p-values and Gaussian significances for the single-bin signal regions are given, along with the 95 % C.L. upper limit on the cross section (in fb), σ, and number of events, N_{BSM}, for non-Standard Model production in each region. The nominal expected limits are shown in parentheses along with the limits in the case of a one-σ upward ($\uparrow$) or downward ($\downarrow$) fluctuation in observation.

8 Conclusion

A search for SUSY in final states containing two leptons with 20.3 fb^{-1} of pp collision data at $\sqrt{s} =$ 8 TeV collected with the ATLAS detector at the LHC has been presented. No significant deviation from the Standard Model background expectation is observed. Upper limits are provided on the visible cross section for BSM event production.

The results are also interpreted in terms of limits on SUSY-inspired simplified models and a minimal universal extra dimensions model. These limits represent an improvement of over 150 GeV relative to the 2011 limits on the same processes [23]. In the two-step decay simplified models, where the fraction of events containing at least two leptons is high, the limits presented here are competitive with those of other ATLAS analyses.

channel	OS $ee/\mu\mu$ SR1	OS $e\mu$ SR1	OS $ee/\mu\mu$ SR2	OS $e\mu$ SR2
Observed events	91	81	7	8
Fitted bkg events	112 ± 16	92 ± 13	10.3 ± 2.6	9.8 ± 2.7
Fitted DibosonWW events	31 ± 8	28 ± 7	0.89 ± 0.25	0.45 ± 0.14
Fitted ZX events	5.1 ± 1.1	1.90 ± 0.15	0.44 ± 0.10	0.10 ± 0.03
Fitted Top events	64 ± 11	53 ± 10	8.6 ± 2.4	8.4 ± 2.3
Fitted reducible bkg. events	11 ± 6	8.9 ± 5	$0.4^{+0.7}_{-0.4}$	$0.8^{+1.1}_{-0.8}$
MC exp. SM events	109	90	11.9	10.1
MC exp. DibosonWW events	29	26	0.84	0.45
MC exp. ZX events	6.3	1.84	0.54	0.10
MC exp. Top events	62	54	10.2	8.7
Exp. reducible bkg. events	11	8.9	0.4	0.8
95 % C.L. upper limit on N_{BSM}	$24\ (33^{\uparrow 45}_{\downarrow 24})$	$25\ (30^{\uparrow 41}_{\downarrow 22})$	$6.1\ (8.2^{\uparrow 11.9}_{\downarrow 5.7})$	$7.3\ (8.3^{\uparrow 12.1}_{\downarrow 5.8})$
95 % C.L. upper limit on σ_{BSM} [fb]	$1.2\ (1.6^{\uparrow 2.2}_{\downarrow 1.2})$	$1.2\ (1.5^{\uparrow 2.0}_{\downarrow 1.0})$	$0.30\ (0.40^{\uparrow 0.59}_{\downarrow 0.28})$	$0.36\ (0.41^{\uparrow 0.59}_{\downarrow 0.29})$
p_0-value (Gauss. σ)	$0.86\ (-1.1)$	$0.73\ (-0.60)$	$0.81\ (-0.88)$	$0.66\ (-0.42)$

Table 9: Observed numbers of events and predictions from the fit to the SM backgrounds in the control regions extrapolated to the OS signal regions, for an integrated luminosity of 20.3 fb^{-1}. Nominal MC expectations (normalised to MC cross sections) are given for comparison. The errors shown are the statistical plus systematic uncertainties. The observed p-values and Gaussian significances for the single-bin signal regions are given, along with the 95 % C.L. upper limit on the cross section (in fb), σ_{BSM}, and number of events, N_{BSM}, for non-Standard Model production in each region. The nominal expected limits are shown in parentheses along with the limits in the case of a one-σ upward ($\uparrow$) or downward ($\downarrow$) fluctuation in observation.
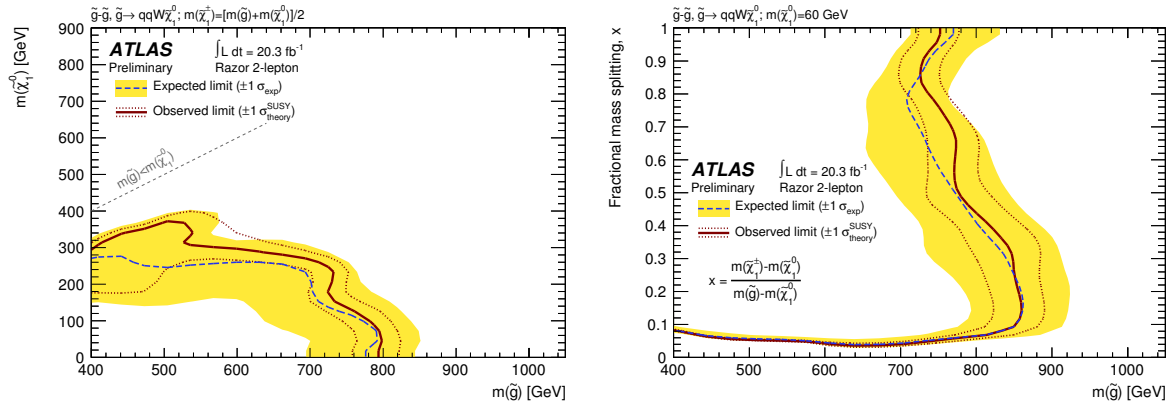

Figure 18: Expected and observed exclusion limits for a simplified model with gluino pair production, where each gluino decays to two quarks and a chargino, and the chargino subsequently decays to a W and the LSP. On the left, in terms of the LSP and gluino mass with the chargino mass fixed to be halfway between the two. On the right, for a fixed LSP mass of 60 GeV.

24

channel	$ee/\mu\mu$ DR	$e\mu$ DR
Observed events	17	12
Fitted bkg events	17.3 ± 2.6	17.8 ± 3.2
Fitted DibosonWW events	5.9 ± 1.3	5.8 ± 1.5
Fitted ZX events	1.52 ± 0.30	0.76 ± 0.11
Fitted Top events	7.7 ± 1.5	7.6 ± 1.7
Fitted reducible bkg. events	1.2 ± 1.2	2.6 ± 1.7
MC exp. SM events	17.6	17.3
MC exp. DibosonWW events	5.6	5.4
MC exp. ZX events	1.83	0.78
MC exp. Top events	8.0	7.6
Exp. reducible bkg events	1.2	2.6
95 % C.L. upper limit on N_{BSM}	$11.0\ (10.4^{\uparrow 15.1}_{\downarrow 7.3})$	$7.6\ (10.4^{\uparrow 15.0}_{\downarrow 7.3})$
95 % C.L. upper limit on σ_{BSM} [fb]	$0.54\ (0.51^{\uparrow 0.74}_{\downarrow 0.36})$	$0.37\ (0.51^{\uparrow 0.74}_{\downarrow 0.36})$
p_0-value (Gauss. σ)	$0.44\ (0.16)$	$0.84\ (-0.98)$

Table 10: Observed numbers of events and predictions from the fit to the SM backgrounds in the control regions extrapolated to the signal regions, for an integrated luminosity of 20.3 fb^{-1}. Nominal MC expectations (normalised to MC cross sections) are given for comparison. The errors shown are the statistical plus systematic uncertainties. The observed p-values and Gaussian significances for the single-bin discovery regions are given, along with the 95 % C.L. upper limit on the cross section (in fb), σ, and number of events, N_{BSM}, for non-Standard Model production in each region. These regions are identical to $ee/\mu\mu$ SR1 and $e\mu$ SR1 but with a higher $M'_R > 600$ GeV requirement. The nominal expected limits are shown in parentheses along with the limits in the case of a one-σ upward ($\uparrow$) or downward ($\downarrow$) fluctuation in observation.
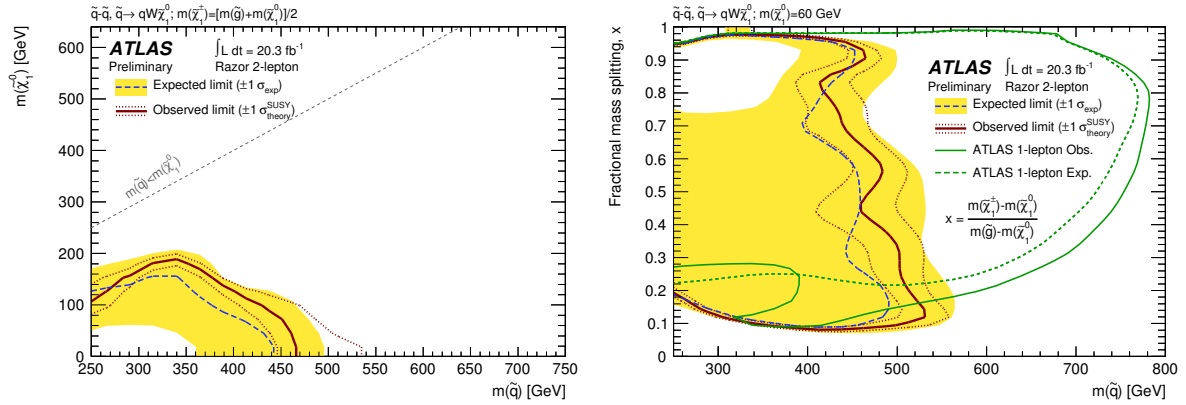

Figure 19: Expected and observed exclusion limits for a simplified model with squark pair production, where each squark decays to a quark and a chargino, and the chargino subsequently decays to a W and the LSP. On the left, in terms of the LSP and squark mass with the chargino mass fixed to be halfway between the two. On the right, for a fixed LSP mass of 60 GeV. The limits from Ref. [18] are overlaid on the right.

channel	OS $ee/\mu\mu$ DR	OS e/μ DR
Observed events	17	10
Fitted bkg events	16.3 ± 2.5	15.6 ± 2.8
Fitted DibosonWW events	5.9 ± 1.3	5.8 ± 1.5
Fitted ZX events	1.17 ± 0.21	0.20 ± 0.03
Fitted Top events	7.4 ± 1.5	7.3 ± 1.6
Fitted reducible bkg. events	$0.9^{+1.0}_{-0.9}$	1.3 ± 1.2
MC exp. SM events	16.4	15.2
MC exp. DibosonWW events	5.6	5.3
MC exp. ZX events	1.41	0.22
MC exp. Top events	7.6	7.3
Exp. reducible bkg events	0.9	1.3
95 % C.L. upper limit on N_{BSM}	$11.6\ (10.2^{\uparrow 14.8}_{\downarrow 7.1})$	$6.8\ (9.6^{\uparrow 13.9}_{\downarrow 6.7})$
95 % C.L. upper limit on σ_{BSM} [fb]	$0.57\ (0.50^{\uparrow 0.73}_{\downarrow 0.35})$	$0.33\ (0.47^{\uparrow 0.68}_{\downarrow 0.33})$
p_0-value (Gauss. σ)	$0.36\ (0.36)$	$0.85\ (-1.1)$

Table 11: Observed numbers of events and predictions from the fit to the SM backgrounds in the control regions extrapolated to the signal regions, for an integrated luminosity of 20.3 fb^{-1}. Nominal MC expectations (normalised to MC cross sections) are given for comparison. The errors shown are the statistical plus systematic uncertainties. The observed p-values and Gaussian significances for the single-bin OS discovery regions are given, along with the 95 % C.L. upper limit on the cross section (in fb), σ, and number of events, N_{BSM}, for non-Standard Model production in each region. These regions are identical to $ee/\mu\mu$ OS SR1 and $e\mu$ OS SR1 but with a higher $M'_R > 600$ GeV requirement. The nominal expected limits are shown in parentheses along with the limits in the case of a one-σ upward ($\uparrow$) or downward ($\downarrow$) fluctuation in observation.
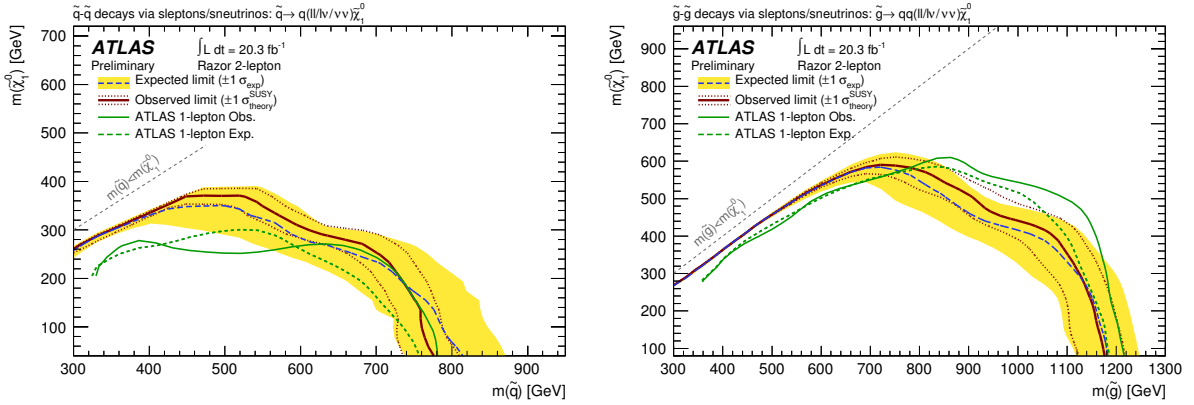

Figure 20: Expected and observed exclusion limits for a simplified model with squark pair production (left) or gluino pair production (right), where each squark (gluino) decays to a quark (two quarks) and chargino, and the chargino subsequently decays through a slepton or sneutrino to the LSP. The limits from Ref. [18] are overlaid.
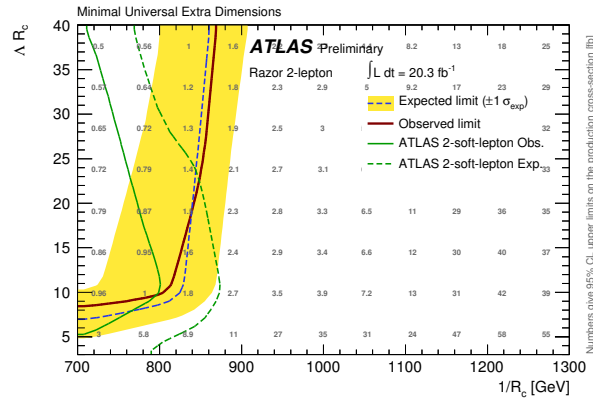
Figure 21: Expected and observed exclusion limits for the minimal universal extra dimensions model. 95 % CL upper limits on the production cross section are shown. The limits from Ref. [18] are overlaid.

References

[1] H. Miyazawa, *Baryon Number Changing Currents*, Prog. Theor. Phys. **36 (6)** (1966) 1266–1276.

[2] P. Ramond, *Dual Theory for Free Fermions*, Phys. Rev. **D3** (1971) 2415–2418.

[3] Y. A. Golfand and E. P. Likhtman, *Extension of the Algebra of Poincare Group Generators and Violation of p Invariance*, JETP Lett. **13** (1971) 323–326. [Pisma Zh. Eksp. Teor. Fiz. 13:452-455,1971].

[4] A. Neveu and J. H. Schwarz, *Factorizable dual model of pions*, Nucl. Phys. **B31** (1971) 86–112.

[5] A. Neveu and J. H. Schwarz, *Quark Model of Dual Pions*, Phys. Rev. **D4** (1971) 1109–1111.

[6] J. Gervais and B. Sakita, *Field theory interpretation of supergauges in dual models*, Nucl. Phys. **B34** (1971) 632–639.

[7] D. V. Volkov and V. P. Akulov, *Is the Neutrino a Goldstone Particle?*, Phys. Lett. **B46** (1973) 109–110.

[8] J. Wess and B. Zumino, *A Lagrangian Model Invariant Under Supergauge Transformations*, Phys. Lett. **B49** (1974) 52.

[9] J. Wess and B. Zumino, *Supergauge Transformations in Four-Dimensions*, Nucl. Phys. **B70** (1974) 39–50.

[10] P. Fayet, *Supersymmetry and Weak, Electromagnetic and Strong Interactions*, Phys. Lett. **B64** (1976) 159.

[11] P. Fayet, *Spontaneously Broken Supersymmetric Theories of Weak, Electromagnetic and Strong Interactions*, Phys. Lett. **B69** (1977) 489.

[12] G. R. Farrar and P. Fayet, *Phenomenology of the Production, Decay, and Detection of New Hadronic States Associated with Supersymmetry*, Phys. Lett. **B76** (1978) 575–579.

[13] P. Fayet, *Relations Between the Masses of the Superpartners of Leptons and Quarks, the Goldstino Couplings and the Neutral Currents*, Phys. Lett. **B84** (1979) 416.

[14] S. Dimopoulos and H. Georgi, *Softly Broken Supersymmetry and SU(5)*, Nucl. Phys. **B193** (1981) 150.

[15] ATLAS Collaboration, *The ATLAS Experiment at the CERN Large Hadron Collider*, JINST **3** (2008) S08003.

[16] L. Evans and P. Bryant (editors), *LHC Machine*, JINST **3** (2008) S08001.

[17] ATLAS Collaboration, *Search for strongly produced superpartners in final states with two same sign leptons with the ATLAS detector using 21 fb^{-1} of proton-proton collisions at $\sqrt{s} = 8$ TeV*, ATLAS-CONF-2013-007 (2013) . http://cds.cern.ch/record/1522430.

[18] ATLAS Collaboration, *Search for squarks and gluinos in events with isolated leptons, jets and missing transverse momentum at $\sqrt{s} = 8$ TeV with the ATLAS detector*, ATLAS-CONF-2013-062 (2013) . http://cds.cern.ch/record/1557779.

[19] ATLAS Collaboration, *Search for Supersymmetry in Events with Large Missing Transverse Momentum, Jets, and at Least One Tau Lepton in 21 fb^{-1} of $\sqrt{s}$ = 8 TeV Proton-Proton Collision Data with the ATLAS Detector*, ATLAS-CONF-2013-026 (2013) . https://cds.cern.ch/record/1525882.

[20] ATLAS Collaboration, *Search for squarks and gluinos with the ATLAS detector in final states with jets and missing transverse momentum and 20.3 fb^{-1} of $\sqrt{s}$=8 TeV proton-proton collision data*, ATLAS-CONF-2013-047 (2013) . http://cds.cern.ch/record/1547563.

[21] ATLAS Collaboration, *Search for new phenomena in final states with large jet multiplicities and missing transverse momentum at $\sqrt{s}$=8 TeV proton-proton collisions using the ATLAS experiment*, arXiv:1308.1841 [hep-ex]. Submitted to JHEP.

[22] C. Rogan, *Kinematical variables towards new dynamics at the LHC*, arXiv:1006.2727 [hep-ph].

[23] ATLAS Collaboration, *Multi-channel search for squarks and gluinos in $\sqrt{s}$=7 TeV proton-proton collisions with the ATLAS Detector*, Eur. Phys. J. **C73** (2013) , arXiv:1212.6149 [hep-ex].

[24] CMS Collaboration, *Inclusive search for supersymmetry using the razor variables in pp collisions at $\sqrt{s}$ = 7 TeV*, arXiv:1212.6961 [hep-ex]. Accepted by Phys. Rev. Lett.

[25] H.-C. Cheng, K. Matchev, and M. Schmaltz, *Bosonic Supersymmetry? Getting Fooled at the LHC*, Phys. Rev. **D66** (2002) 56006.

[26] ATLAS Collaboration, *The ATLAS Simulation Infrastructure*, Eur. Phys. J. **C70** (2010) 823–874, arXiv:1005.4568 [physics.ins-det].

[27] GEANT4 Collaboration, *GEANT4: A Simulation toolkit*, Nucl. Instrum. Meth. **A506** (2003) 250–303.

[28] T. Sjostrand, S. Mrenna, and P. Skands, *A Brief Introduction to PYTHIA 8.1*, Comput. Phys. Commun. **178** (2008) 852, arXiv:0710.3820 [hep-ph].

[29] ATLAS Collaboration, *Further ATLAS tunes of PYTHIA6 and Pythia 8*, ATLAS-PHYS-PUB-2011-014, 2011. http://cds.cern.ch/record/1400677.

[30] A. Martin, W. Stirling, R. Thorne, and G. Watt, *Parton distributions for the LHC*, Eur. Phys. J. **C63** (2009) 189–285, arXiv:0901.0002 [hep-ph].

[31] J. Alwall et al., *MadGraph 5 : Going Beyond*, JHEP **1106** (2011) 128, arXiv:1106.0522 [hep-ph].

[32] S. M. T. Sjostrand and P. Skands, *PYTHIA 6.4 physics and manual*, JHEP **05** (2006) 026, arXiv:hep-ph/0603175.

[33] J. Pumplin et al., *New generation of parton distributions with uncertainties from global QCD analysis*, JHEP **0207** (2002) 012, arXiv:hep-ph/0201195 [hep-ph].

[34] W. Beenakker, R. Hopker, M. Spira, and P. Zerwas, *Squark and gluino production at hadron colliders*, Nucl. Phys. **B492** (1997) 51–103, arXiv:hep-ph/9610490 [hep-ph].

[35] A. Kulesza and L. Motyka, *Threshold resummation for squark-antiquark and gluino-pair production at the LHC*, Phys. Rev. Lett. **102** (2009) 111802, arXiv:0807.2405 [hep-ph].

[36] A. Kulesza and L. Motyka, *Soft gluon resummation for the production of gluino-gluino and squark-antisquark pairs at the LHC*, Phys. Rev. **D80** (2009) 095004, `arXiv:0905.4749 [hep-ph]`.

[37] W. Beenakker et al., *Soft-gluon resummation for squark and gluino hadroproduction*, JHEP **0912** (2009) 041, `arXiv:0909.4418 [hep-ph]`.

[38] W. Beenakker et al., *Squark and gluino hadroproduction*, Int. J. Mod. Phys. **A26** (2011) 2637–2664, `arXiv:1105.1110 [hep-ph]`.

[39] M. Kramer et al., *Supersymmetry production cross sections in pp collisions at sqrts = 7 TeV*, `arXiv:1206.2892 [hep-ph]`.

[40] M. Bahr et al., *Herwig++ Physics and Manual*, Eur. Phys. J. **C58** (2008) 639–707, `arXiv:0803.0883 [hep-ph]`.

[41] S. Gieseke, C. Rohr, and A. Siodmok, *Colour reconnections in Herwig++*, Eur. Phys. J. **C72** (2012) 2225, `arXiv:1206.0041 [hep-ph]`.

[42] G. Corcella et al., *HERWIG 6: An Event generator for hadron emission reactions with interfering gluons (including supersymmetric processes)*, JHEP **0101** (2001) 010, `arXiv:hep-ph/0011363 [hep-ph]`.

[43] J. Butterworth, J. R. Forshaw, and M. Seymour, *Multiparton interactions in photoproduction at HERA*, Z. Phys. **C72** (1996) 637–646, `arXiv:hep-ph/9601371 [hep-ph]`.

[44] S. Frixione and B. R. Webber, *Matching NLO QCD computations and parton shower simulations*, JHEP **0206** (2002) 029, `arXiv:hep-ph/0204244 [hep-ph]`.

[45] S. Frixione, P. Nason, and G. Ridolfi, *A Positive-Weight Next-to-Leading-Order Monte Carlo for Heavy Flavour Hadroproduction*, JHEP **0709** (2007) 126, `arXiv:hep-ph/0707.3088`.

[46] B. P. Kersevan and E. Richter-Was, *The Monte Carlo event generator AcerMC version 2.0 with interfaces to PYTHIA 6.2 and HERWIG 6.5*, `arXiv:hep-ph/0405247 [hep-ph]`.

[47] H.-L. Lai et al., *New parton distributions for collider physics*, Phys. Rev. **D82** (2010) 074024, `arXiv:1007.2241 [hep-ph]`.

[48] T. Gleisberg et al., *Event generation with Sherpa 1.1*, JHEP **02** (2009) 007, `0811.4622 [hep-ph]`.

[49] ATLAS Collaboration, *New ATLAS event generator tunes to 2010 data*, ATL-PHYS-PUB-2011-008 (2011) . http://cdsweb.cern.ch/record/1345343.

[50] S. Catani et al., Phys. Rev. Lett. **103** 082001 (2009), `arXiv:0903.2120 [hep-ph]`; S. Catani, M. Grazzini, Phys. Rev. Lett. **98** 222002 (2007) `hep-ph/0703012`.

[51] A. Martin, W. Stirling, R. Thorne, and G. Watt, *Update of parton distributions at NNLO*, Phys. Lett. **B652** (2007) 292–299, `arXiv:0706.0459 [hep-ph]`.

[52] J. M. Campbell, R. Ellis, and D. L. Rainwater, *Next-to-leading order QCD predictions for W + 2 jet and Z + 2 jet production at the CERN LHC*, Phys. Rev. **D68** (2003) 094021, `arXiv:hep-ph/0308195 [hep-ph]`.

[53] M. Cacciari et al., *Top-pair production at hadron colliders with next-to-next-to-leading logarithmic soft-gluon resummation*, Phys. Lett. **B710** (2012) 612–622, `arXiv:1111.5869 [hep-ph]`.

[54] P. Bärnreuther et al., *Percent Level Precision Physics at the Tevatron: First Genuine NNLO QCD Corrections to $q\bar{q} \to t\bar{t}$*, Phys. Rev. Lett. **109** (2012) 132001, `arXiv:1204.5201 [hep-ph]`.

[55] M. Czakon and A. Mitov, *NNLO corrections to top-pair production at hadron colliders: the all-fermionic scattering channels*, JHEP **1212** (2012) 054, `arXiv:1207.0236 [hep-ph]`.

[56] M. Czakon and A. Mitov, *NNLO corrections to top pair production at hadron colliders: the quark-gluon reaction*, JHEP **1301** (2013) 080, `arXiv:1210.6832 [hep-ph]`.

[57] M. Czakon, P. Fiedler, and A. Mitov, *The total top quark pair production cross-section at hadron colliders through $O(\alpha_S^4)$*, `arXiv:1303.6254 [hep-ph]`.

[58] M. Czakon and A. Mitov, *Top++: a program for the calculation of the top-pair cross-section at hadron colliders*, `arXiv:1112.5675 [hep-ph]`.

[59] N. Kidonakis, *Next-to-next-to-leading-order collinear and soft gluon corrections for t-channel single top quark production*, Phys. Rev. **D83** (2011) 091503.

[60] N. Kidonakis, *NNLL resummation for s-channel single top quark production*, Phys. Rev. **D81** (2010) 054028.

[61] N. Kidonakis, *Two-loop soft anomalous dimensions for single top quark associated production with a W- or H-*, Phys. Rev. **D82** (2010) 054018.

[62] J. M. Campbell and R. K. Ellis, *$t\bar{t}W$ production and decay at NLO*, JHEP **1207** (2012) 052, `arXiv:hep-ph/1204.5678 [hep-ph]`.

[63] A. Lazopoulos, T. McElmurry, K. Melnikov, and F. Petriello, *Next-to-leading order QCD corrections to t-tbar-Z production at the LHC*, Phys. Lett. **B666** (2008) 62, `arXiv:hep-ph/0804.2220 [hep-ph]`.

[64] ATLAS Collaboration, *Electron performance measurements with the ATLAS detector using the 2010 LHC proton-proton collision data*, `arXiv:1110.3174 [hep-ex]`.

[65] ATLAS Collaboration, *A measurement of the ATLAS muon reconstruction and trigger efficiency using J/psi decays*, ATLAS-CONF-2011-021 (2011) . http://cdsweb.cern.ch/record/1336750.

[66] ATLAS Collaboration, *Muon reconstruction efficiency in reprocessed 2010 LHC proton-proton collision data recorded with the ATLAS detector*, ATLAS-CONF-2011-063 (2011) . http://cdsweb.cern.ch/record/1345743.

[67] M. Cacciari, G. P. Salam, and G. Soyez, *The anti-k_t jet clustering algorithm*, JHEP **04** (2008) 063, `arXiv:0802.1189 [hep-ph]`.

[68] M. Cacciari and G. P. Salam, *Dispelling the N^3 myth for the k_t jet-finder*, Phys. Lett. **B641** (2006) 57–61, `arXiv:hep-ph/0512210`.

[69] ATLAS Collaboration, *Expected Performance of the ATLAS Experiment - Detector, Trigger and Physics*, `arXiv:0901.0512 [hep-ex]`.

[70] ATLAS Collaboration, *Commissioning of the ATLAS high-performance b-tagging algorithms in the 7 TeV collision data*, ATLAS-CONF-2011-102 (2011) . http://cdsweb.cern.ch/record/1369219.

[71] ATLAS Collaboration, *Jet energy measurement with the ATLAS detector in proton-proton collisions at $\sqrt{s}$ = 7 TeV*, Eur. Phys. J. **C73** (2013) 2304, `arXiv:1112.6426 [hep-ex]`.

[72] ATLAS Collaboration, *Single hadron response measurement and calorimeter jet energy scale uncertainty with the ATLAS detector at the LHC*, Eur. Phys. J. **C73** (2013) 2305, `arXiv:1203.1302 [hep-ex]`.

[73] ATLAS Collaboration, *Jet energy resolution and selection efficiency relative to track jets from in-situ techniques with the ATLAS Detector Using Proton-Proton Collisions at a Center of Mass Energy $\sqrt{s}$ = 7 TeV*, ATLAS-CONF-2010-054 (2010) . http://cdsweb.cern.ch/record/1281311.

[74] ATLAS Collaboration, *Measurement of the b-tag Efficiency in a Sample of Jets Containing Muons with 5 fb^{-1} of Data from the ATLAS Detector*, ATLAS-CONF-2012-043 (2012) . http://cdsweb.cern.ch/record/1435197.

[75] ATLAS Collaboration, *Measurement of the Mistag Rate of b-tagging algorithms with 5 fb^{-1} of Data Collected by the ATLAS Detector*, ATLAS-CONF-2012-040 (2012) . http://cdsweb.cern.ch/record/1435194.

[76] ATLAS Collaboration, *Search for direct production of charginos and neutralinos in events with three leptons and missing transverse momentum in 21 fb^{-1} of pp collisions at $\sqrt{s}$ = 8 TeV with the ATLAS detector*, ATLAS-CONF-2013-035 (2013) . http://cds.cern.ch/record/1532426.

[77] S. Frixione et al., *Single-top hadroproduction in association with a W boson*, JHEP **0807** (2008) 029, `arXiv:0805.3067 [hep-ph]`.

[78] P. Artoisenet et al., *A framework for Higgs characterisation*, `arXiv:1306.6464 [hep-ph]`. See also http://amcatnlo.web.cern.ch/amcatnlo/.

[79] ATLAS Collaboration, *Search for supersymmetry in final states with jets, missing transverse momentum and one isolated lepton in $\sqrt{s}$ = 7 TeV pp collisions using 1 fb^{-1} of ATLAS data*, Phys. Rev. **D85** (2011) 012006, `arXiv:1109.6606 [hep-ex]`.

[80] ATLAS Collaboration, *Improved luminosity determination in pp collisions at $\sqrt{s}$ = 7 TeV using the ATLAS detector at the LHC*, `arXiv:1302.4393 [hep-ex]`. Accepted by Eur. Phys. J. C.

[81] G. Cowan, K. Cranmer, E. Gross, and O. Vitells, *Asymptotic formulae for likelihood-based tests of new physics*, Eur. Phys. J. **C71** (2011) 1554, `arXiv:1007.1727 [physics.data-an]`.

[82] A. L. Read, *Presentation of search results: The CL(s) technique*, J. Phys. **G28** (2002) 2693–2704.

A   Cutflow table

This section includes a table showing the unweighted number of MC events surviving each stage of the cutflow for this analysis. The benchmark point chosen for this in the gluino-gluino one-step simplified model with $m_{\tilde{g}} = 800$ GeV, $m_{\tilde{\chi}_1^\pm} = 460$ GeV and $m_{LSP} = 60$ GeV. The cutflow can be found in Table 12.

channel	*ee*	*μμ*	*eμ*
No cuts		59999	
Exactly two baseline leptons		2073	
Passes trigger requirements		1670	
Di-lepton invariant mass > 20 GeV		1639	
Lepton flavour separation	576	397	666
Leptons satisfy signal lepton requirements	443	373	549
Trigger + 2 lepton selection requirements	429	358	517
> 2 jets (p_T > 50 GeV), *b*-veto	341	297	424
Z-veto (81 < $m_{\ell\ell}$ < 101 GeV)	319	276	N/A
R > 0.35	139	137	195
M_R' > 800 GeV	53	50	63
< 3 jets (p_T > 50 GeV), *b*-veto	53	40	54
Z-veto (81 < $m_{\ell\ell}$ < 101 GeV)	51	36	N/A
R > 0.5	16	19	12
M_R' > 400 GeV	14	19	10

Table 12: Cutflow table for an example gluino-gluino one-step benchmark point with $m_{\tilde{g}} = 800$ GeV, $m_{\tilde{\chi}_1^\pm} = 460$ GeV, $m_{LSP} = 60$.

B   Cross section upper limits

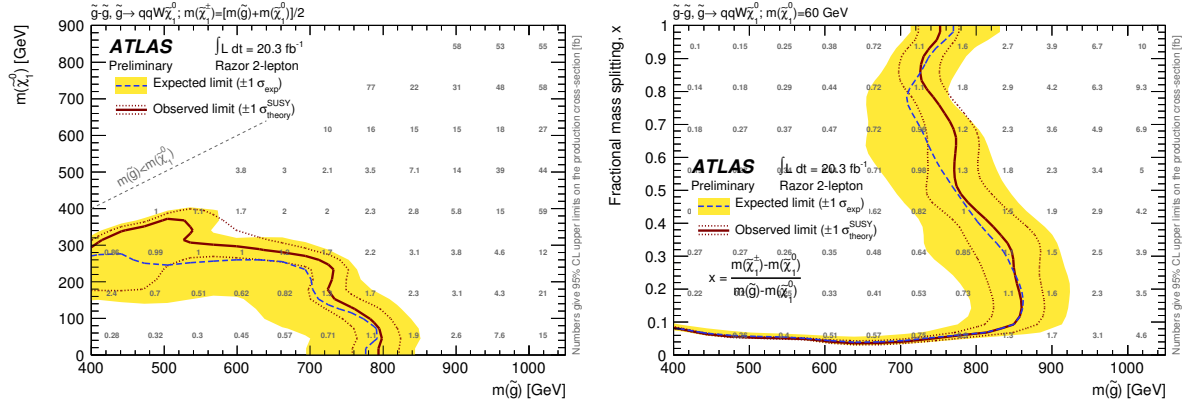Here the exclusion figures are shown with cross-section upper limits included.

Figure 22: Expected and observed exclusion limits for a simplified model with gluino pair production, where each gluino decays to two quarks and a chargino, and the chargino subsequently decays to a W and the LSP. On the left, in terms of the LSP and gluino mass with the chargino mass fixed to be half-way between the two. On the right, for a fixed LSP mass of 60 GeV. 95% CL upper limits on the production cross section are shown.
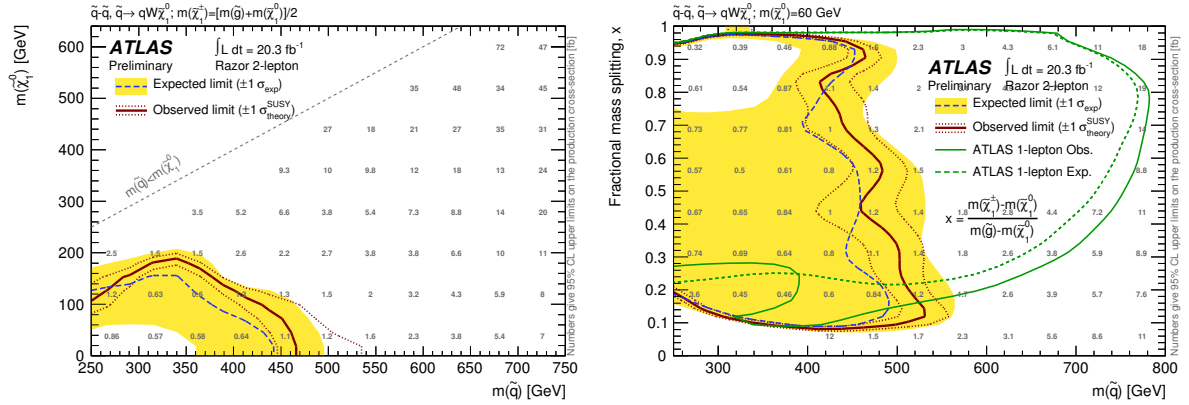

Figure 23: Expected and observed exclusion limits for a simplified model with squark pair production, where each squark decays to a quark and a chargino, and the chargino subsequently decays to a W and the LSP. On the left, in terms of the LSP and squark mass with the chargino mass fixed to be half-way between the two. On the right, for a fixed LSP mass of 60 GeV. The limits from Ref. [18] are overlaid on the right. 95% CL upper limits on the production cross section are shown.
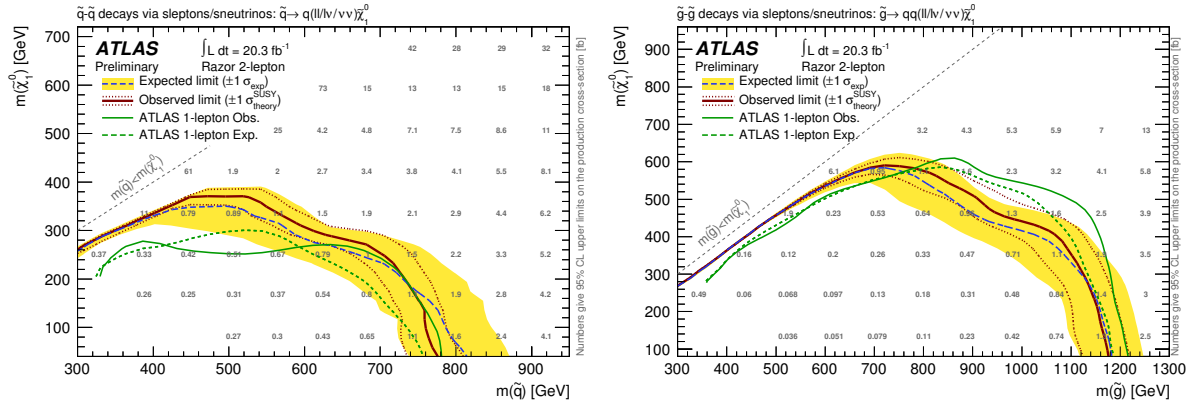
34

Figure 24: Expected and observed exclusion limits for a simplified model with squark pair production (left) or gluino pair production (right), where each squark (gluino) decays to a quark (two quarks) and chargino, and the chargino subsequently decays through a slepton or sneutrino to the LSP. The limits from Ref. [18] are overlaid. 95% CL upper limits on the production cross section are shown.